

# **Coupled Thermal-Hydrologic- Chemical Model for In-Drift Disposal Test**

**Fuel Cycle Research & Development**

*Prepared for  
U.S. Department of Energy  
Used Fuel Disposition Campaign  
Milestone M4FT-15LA0819015*

*A.B Jordan, G.A. Zyvoloski, D.J. Weaver, S. Otto, P.H. Stauffer  
Los Alamos National Laboratory  
September 25, 2015*

**Los Alamos National Laboratory Document  
LA-UR-15-27442**



**DISCLAIMER**

This information was prepared as an account of work sponsored by an agency of the U.S. Government. Neither the U.S. Government nor any agency thereof, nor any of their employees, makes any warranty, expressed or implied, or assumes any legal liability or responsibility for the accuracy, completeness, or usefulness, of any information, apparatus, product, or process disclosed, or represents that its use would not infringe privately owned rights. References herein to any specific commercial product, process, or service by trade name, trade mark, manufacturer, or otherwise, does not necessarily constitute or imply its endorsement, recommendation, or favoring by the U.S. Government or any agency thereof. The views and opinions of authors expressed herein do not necessarily state or reflect those of the U.S. Government or any agency thereof.


**FCT Quality Assurance Program Document**

**Appendix E  
 FCT Document Cover Sheet**

LANL Report entitled - " Coupled Thermal-Hydrologic-Chemical Coupled Model for In-Drift Disposal Test "

DR Salt Field Testing – LANL, FT-15LA081901

**1.02.08.19**

Philip Stauffer  
 (Name/Signature) 

Date Submitted September 25, 2015

Quality Rigor Level for Deliverable/Milestone	<input checked="" type="checkbox"/> QRL-3	<input type="checkbox"/> QRL-2	<input type="checkbox"/> QRL-1 <input type="checkbox"/> Nuclear Data	<input type="checkbox"/> N/A*
---	---	--------------------------------	---	-------------------------------

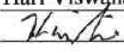
This deliverable was prepared in accordance with Los Alamos National Laboratory  
 (Participant/National Laboratory Name)

QA program which meets the requirements of  
 DOE Order 414.1       NQA-1-2000

**This Deliverable was subjected to:**

<input type="checkbox"/> Technical Review	<input checked="" type="checkbox"/> Peer Review
<b>Technical Review (TR)</b>	<b>Peer Review (PR)</b>
<b>Review Documentation Provided</b>	<b>Review Documentation Provided</b>
<input type="checkbox"/> Signed TR Report or,	<input type="checkbox"/> Signed PR Report or,
<input type="checkbox"/> Signed TR Concurrence Sheet or,	<input type="checkbox"/> Signed PR Concurrence Sheet or,
<input type="checkbox"/> Signature of TR Reviewer(s) below	<input checked="" type="checkbox"/> Signature of PR Reviewer(s) below

**Name and Signature of Reviewers**

Hari Viswanathan 

\*Note: In some cases there may be a milestone where an item is being fabricated, maintenance is being performed on a facility, or a document is being issued through a formal document control process where it specifically calls out a formal review of the document. In these cases, documentation (e.g., inspection report, maintenance request, work planning package documentation or the documented review of the issued document through the document control process) of the completion of the activity along with the Document Cover Sheet is sufficient to demonstrate achieving the milestone. QRL for such milestones may be also be marked N/A in the work package provided the work package clearly specifies the requirement to use the Document Cover Sheet and provide supporting documentation.

## TABLE OF CONTENTS

<b>1. INTRODUCTION.....</b>	<b>1</b>
<b>2. FEHM UPDATES.....</b>	<b>1</b>
2.1 Enhancements to the Air-Water-Heat Physics Module.....	1
2.2 Salt Controller Module.....	2
2.3 Code Testing.....	3
<b>3. BENCH-SCALE MODELING.....</b>	<b>5</b>
3.1 Experiment Description.....	5
3.2 Model Setup.....	8
3.3 Results.....	11
3.3.1 Experiment 0.....	11
3.3.2 Experiment 1.....	15
3.3.3 Experiment 2.....	18
<b>4. HEATER TEST MODELING.....</b>	<b>20</b>
<b>5. HYDROUS MINERAL DEHYDRATION AROUND HEAT-GENERATING NUCLEAR WASTE IN BEDDED SALT FORMATIONS (PUBLISHED).....</b>	<b>23</b>
<b>6. FUTURE WORK.....</b>	<b>31</b>
<b>REFERENCES.....</b>	<b>32</b>
<b>APPENDIX A: NGAS AND BOUN USAGE.....</b>	<b>35</b>
<b>APPENDIX B: SALT CONTROLLER MODULE USAGE.....</b>	<b>40</b>

## LIST OF FIGURES

Figure 1. Numerical mesh for the salt box experiment.....	4
Figure 2. Saturation difference between (a) 0.1 and 0 days, and (b) 5 and 0 days.....	4
Figure 3. Total water loss and water flow rate for a flow-only, coarse-mesh model. ....	5
Figure 4. Salt box, data loggers, and multi-gas monitor. ....	6
Figure 5. Schematic of the experimental setup. ....	7
Figure 6. Location of thermocouple bundles. ....	7
Figure 7. Zones in the numerical mesh used for modeling the laboratory experiment.....	9
Figure 8. Numerical mesh for the model of Experiment 0. ....	11
Figure 9. Simulated chloroform concentrations 3 seconds after injection.....	12
Figure 10. Experiment 0 tracer test data and model comparison. ....	13
Figure 11. Saturation with depth in granular salt ( $t = 30$ days): Model vs data.....	14
Figure 12. Saturation in the model after 30 days. ....	15
Figure 13. Numerical mesh for the model of Experiment 1. ....	16
Figure 14. Chloroform data from Experiment 1, cool pre-test run (T1).....	17
Figure 15. Temperature profile with depth for Experiment 1: Model vs Data .....	18
Figure 16. Numerical mesh for the model of Experiment 2. ....	19
Figure 17. Prototype canister heater.....	20
Figure 18. Heating harness inserted into canister. ....	20
Figure 19. Numerical mesh of the prototype canister heater. ....	21
Figure 20. Temperature test data from the prototype canister. ....	22
Figure 21. Temperature: Prediction vs Data for the 1250W prototype canister. ....	23

## LIST OF TABLES

Table 1. Dimensions and locations of apparatus in the salt laboratory experiments.....	8
Table 2. Simulation parameters for all modeled experiments.....	10
Table 3. Experiment 0 initial and boundary conditions. ....	11
Table 4. Tracer information for E0. ....	12
Table 5. E1 initial and boundary conditions. ....	16
Table 6. E2 initial and boundary conditions. ....	19
Table 7. New usage of the FEHM <i>ngas</i> macro. ....	35
Table 8. Annotated examples of the updated <i>ngas</i> and <i>boun</i> macros.....	36
Table 9. Description of changes to FEHM source code files. ....	39
Table 10. Usage of keyword <i>saltppor</i> . ....	40
Table 11. Usage of keyword <i>saltvcon</i> . ....	40
Table 13. Usage of keyword <i>saltadif</i> . ....	41
Table 14. Usage of keyword <i>saltvapr</i> . ....	41
Table 14. Usage of keyword <i>saltnum</i> . ....	42
Table 15. Usage of keyword <i>saltend</i> . ....	42

## **Coupled Thermal-Hydrologic-Chemical Model for In-Drift Disposal Test**

### **1. Introduction**

The simulation work presented in this report supports DOE-NE Used Fuel Disposition Campaign (UFDC) goals related to the development of drift scale in-situ field testing of heat generating nuclear waste (HGNW) in salt formations. Numerical code verification and validation is an important part of the lead-up to field testing, allowing exploration of potential heater emplacement designs, monitoring locations, and perhaps most importantly the ability to predict heat and mass transfer around an evolving test. Such predictions are crucial for the design and location of sampling and monitoring that can be used to validate our understanding of a drift scale test that is likely to span several years.

Many of the process level calculations and code developments presented herein are tied to experimental work that is described in Jordan et al., (2014, 2015) and Stauffer et al., (2015). One of the major experimental objectives was to collect data that could be used to validate models of the physiochemical processes and hydrologic parameters relevant to moist, heated run-of-mine (RoM) salt. In a feedback loop between the numerical model, laboratory experiments and field-scale experiments, experimental results will be used to validate the model, while the model will be used to interpret the field results. Together, the experiments and models will be the key to understanding the processes and evolution of a system for disposal of HGNW in bedded salt formations.

Simulations described in this report are built using the Finite Element Heat and Mass Transfer Code (FEHM). This code has been developed at LANL for over 30 years (Zyvoloski, 1997, 2007) and started as a tool to simulate geothermal reservoirs as part of LANL's groundbreaking Hot Dry Rock geothermal energy program (Kelkar et al., 2011), but has grown over the years to include unsaturated flow, reactive chemistry, stress, and carbon dioxide (<https://fehm.lanl.gov>). FEHM uses a finite volume method for solving multiphase flow and transport, while using a finite element formulation for the fully coupled stress solutions. Capabilities pertinent to simulations in salt are presented in Stauffer et al. (2013). In Section 2 of this milestone, we describe additions to FEHM that allow better simulation of airflow in fully coupled thermal/hydrological/chemical problems. These additions to the code are necessary for accurate modeling of ventilated drift-scale heated salt simulations, as well as the bench-scale laboratory experiments described in Section 3. Section 4 describes initial modeling associated with a full scale prototype waste canister containing embedded heaters to represent HGNW. The prototype was built through a collaboration between LANL, and Stoller with the purpose of gaining knowledge about canister fabrication and initial thermal testing (Stoller, 2014). Section 5 presents a 2015 publication related to model updates for including hydrous mineral dehydration.

### **2. FEHM Updates**

#### **2.1 Enhancements to the Air-Water-Heat Physics Module**

Several modifications were made to the air-water-heat physics module of FEHM that is invoked with the *ngas* control statement (Zyvoloski et al., 1997). These were made to improve

the performance of FEHM when simulating the dry-out of rock. Initial testing shows a very good improvement in performance. Key additions to capability include:

1. The ability to set a fixed total pressure with a flowing mass fraction of air: This is useful when applying a high pressure source of low humidity air to dry reservoir rock. Available in *ngas* macro and *boun* macro.
2. Improved ability to simulate a constant saturation node by allowing both fixed saturation and fixed pressure at the node: The simulated physics allows the saturation to be maintained at a fixed value by addition/removal of water. The pressure is maintained by the addition/removal of air in the vapor phase. Because the vapor phase contains water vapor and air, this by itself can dry out the rock.
3. The outflow fluid mixture with constant pressure was corrected to include the correct mixture of air and water.
4. The boundary conditions for air-water-heat physics are now available within the *boun* control statement. New keyword 'fxa' for flowing *ngas* mass fraction added. This keyword apportions incoming flow when the flow arises from a fixed pressure condition. Several errors in other *ngas* boundary conditions also now work.

The ability to fix flowrates for both air and water remains unchanged. The humidity boundary condition is changed to a saturation condition using the van Genuchten capillary pressure function. The new usage of the *ngas* macro is given in Appendix A.

## 2.2 Salt Controller Module

A new controller module (*saltctr.f*) was created to manage simulations with salt. This was implemented for three primary reasons: first, to isolate the added salt-related beta version software modifications (Stauffer et al., 2013) into one location so that those modifications can be merged with the primary FEHM software suite and allow a platform for future software development. Second, to easily allow (via user input) different salt capabilities to be tested separately to assess individual process (e.g. porosity change) importance and sensitivity. Third, to allow the testing of numerical algorithms associated with the averaging and temporal updating of the highly nonlinear salt-related physics. This new module was tested to insure that the resulting code produced exactly the same numerical output when compared with software modified by Stauffer and Harp. Key additions to capability include:

1. The ability to run salt simulations with a variety of combinations of water vapor formulations with vapor pressure lowering with different salt concentrations and capillary pressure vapor pressure lowering.
2. The option to initialize grid blocks to saturation temperature at total fluid pressure or total fluid pressure at saturation temperature. The partial pressure of air in these conditions was set to a prescribed small number.
3. Improved numerical performance with temporal averaging of porosities and permeabilities. This simple change allowed significantly smaller porosities to be reached in a simulation while maintaining large time steps. It also was the difference between simulations finishing and not finishing for some parameter combinations.
4. The Sparrow (2003) vapor pressure model that includes the effect of salt has been removed in favor of a fitted function that is used with the original FEHM vapor pressure



model. The modified formulations allows vapor pressure lowering from both salt concentration and capillary pressure.

The salt algorithm behaves as follows. At timestep  $n$  and simulation time  $days$ :

1. Solve coupled equations for pressure, temperature, vapor pressure, and saturation.
2. Save the inter-nodal flowrates for liquid and vapor phases.
3. Solve the tracer transport equations from timestep  $n-1$  to  $n$  (time =  $days$ ). The transport equations are solved at smaller timesteps than the flow equation. The flow rates at time =  $days$ , obtained in step 1, is used for the transport solution.
  - a. At every transport equation evaluate the chemical reactions and quantify precipitation or dissolution of salt and change the porosity.
  - b. From the porosity change, evaluate the permeability change
4. Update flow equation properties, go step 1.

The input structure for the SALT module is similar to that of CO<sub>2</sub> and stress modules in FEHM. That is, it makes use of sub-keywords within the SALT input section. This module allows input that is also available from other keywords (*ppor*, *adif*, *vapl*) but is logically included here as well. Input description and usage is provided in Appendix B.

## 2.3 Code Testing

The code modifications were tested on a mesh developed for the salt box experiments (Section 3). Both a fine mesh and a coarser mesh were tested. Results were in good agreement between the two meshes when the salt material model was not used (referred to here as the “flow only” case). The coarse mesh is shown in Figure 1, along with initial porosity and saturation. The model represents a quarter-space with reflection boundaries on the XZ and YZ faces. Figure 1 shows material zones and the initial layer of ponded water. The mesh is cut away to show the top of the tank; air nodes above are hidden with (a) Porosity at  $t = 0$  days. (b) Saturation at  $t = 0$  days. The node with air inflow is at the center of the box at the top of the airspace above the salt, while the node represented as outflow in the model is at the center, upper edge of the airspace (Figure 1a).

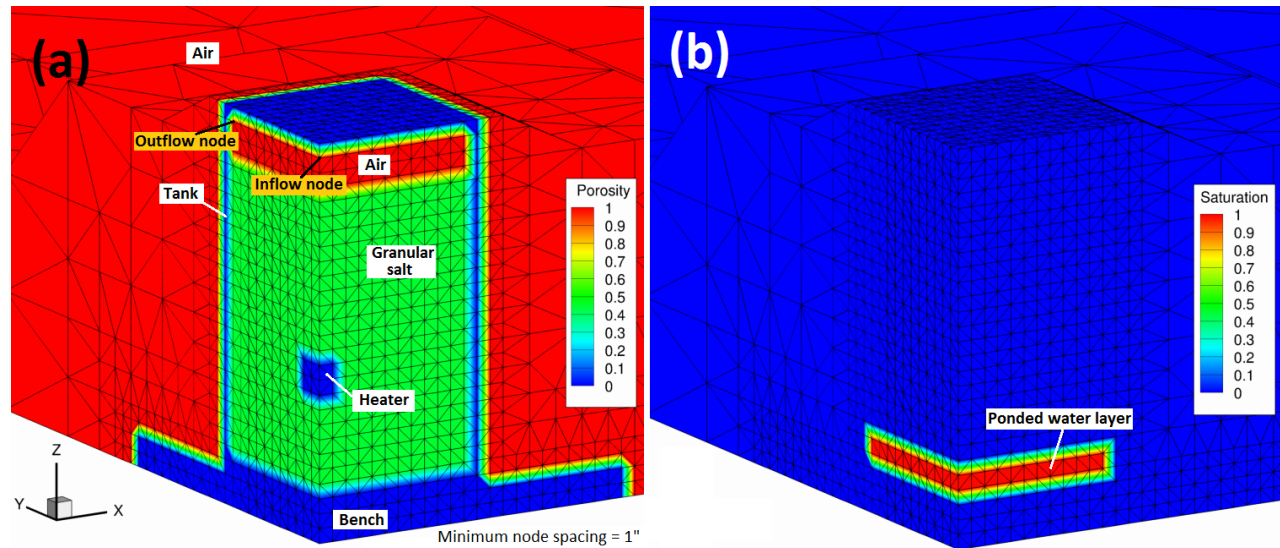


Figure 1. Numerical mesh for the salt box experiment

The difference in saturation between the initial case (Figure 1b) and after 0.1 and 5 days of airflow and heating at 260°C is shown in Figure 2. Immediately after the simulation begins, capillary suction draws the water slightly upwards from the pondered water layer (see Section 3), resulting in the fringe shown in Figure 2a. After additional heating and airflow for up to 5 days, moisture movement through the box is evident in the higher saturations (red) along the box edges (for which evidence is also seen in the experiments by the buildup of a crust along the corners) and reduced saturation (blue) in the pondered water layer (Figure 2b).

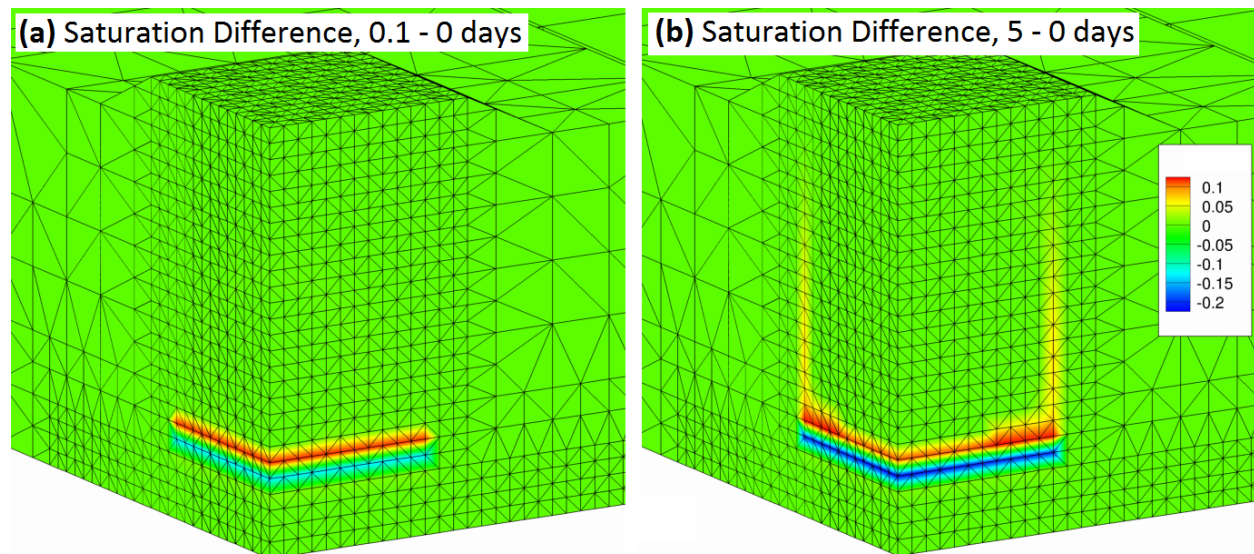


Figure 2. Saturation difference between (a) 0.1 and 0 days, and (b) 5 and 0 days.

Figure 3 shows water loss and water flow rate as a function of time for scenarios ranging from heater temperature of 120°C to 260°C. As expected, higher temperatures result in greater

net water discharge from the box. The initial flow rates vary somewhat non-monotonically but the late-time discharge behavior is generally as expected.

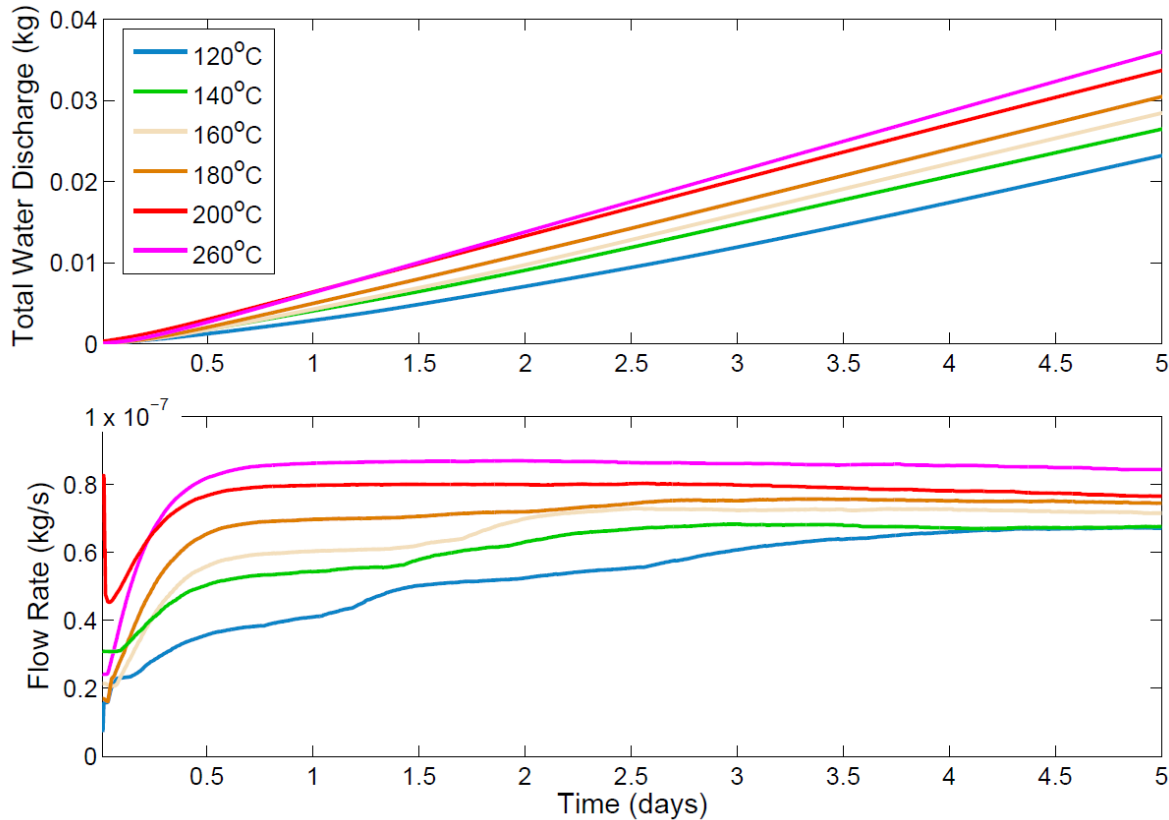


Figure 3. Total water loss and water flow rate for a flow-only, coarse-mesh model.

### 3. Bench-Scale Modeling

#### 3.1 Experiment Description

The Draft Test Plan for Brine Migration Experimental Studies in Run-of-Mine Salt Backfill (Jordan et al., 2014) was developed to identify key experimental objectives related to coupled thermal/hydrological/chemical processes in heated RoM salt. One goal was to provide a data set for comparison with the FEHM salt material model that would explore complex issues including porosity change, airflow and evaporation, and potential heat pipe behavior. The experimental effort took place from December 2014 to August 2015 and is described in Jordan et al., 2015.

The experimental setup is pictured in Figure 4 and diagrammed in Figure 5. In Figure 5, some measurements are not indicated because the placement of components varied between experiments. Figure 6 shows a top-down view of the experimental box after the thermocouples were inserted. Two main experiments were performed. In Experiment 1, the heater was 15 cm (5.9 in.) above the ponded water line and set to 260°C. For Experiment 2 the heater was 5 cm (2.0 in.) above the water and set to 200°C. Table 1 lists certain dimensions of the two main experiments. In Figure 6, bundle A is 1 in. from the heater's long edge; B is 3.25 in.; and C is 6.75 in.



Figure 4. Salt box, data loggers, and multi-gas monitor.

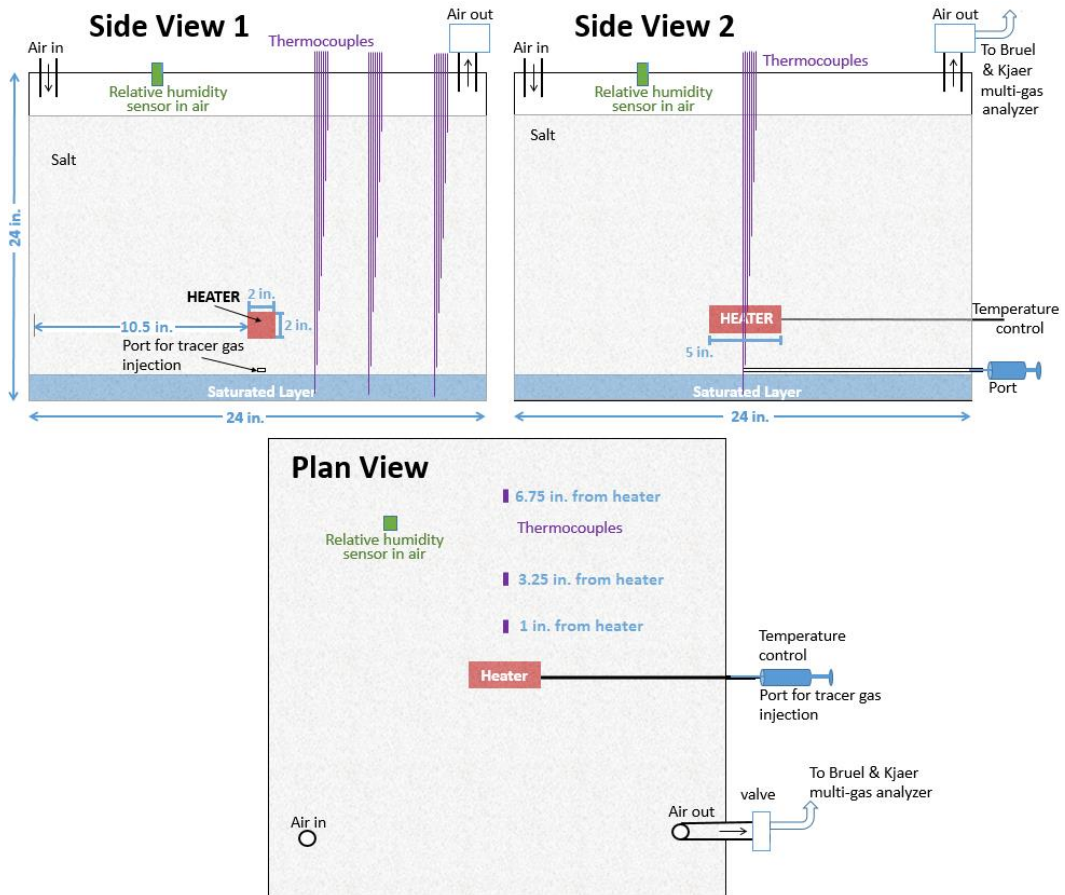


Figure 5. Schematic of the experimental setup.

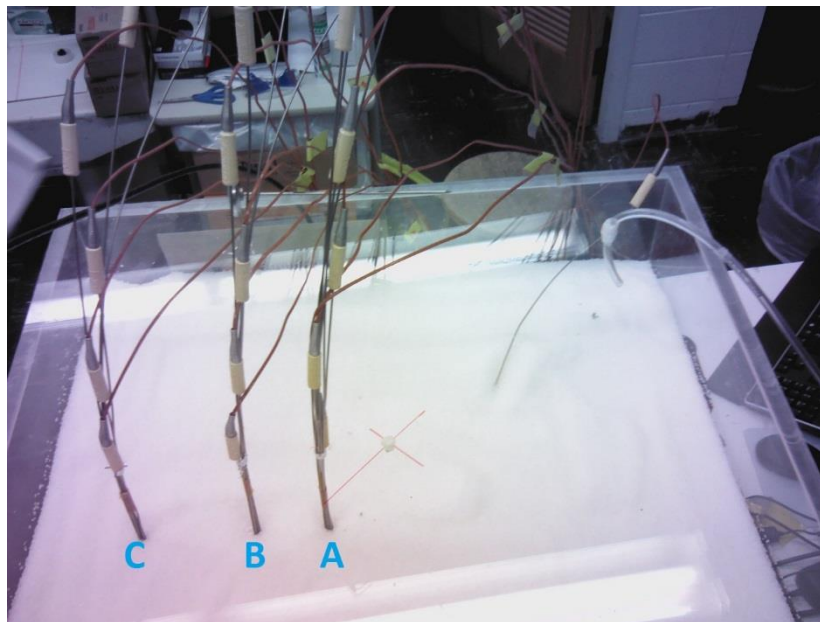


Figure 6. Location of thermocouple bundles.

Object	Dimensions/Location
Box	Outer dimensions L x W x H = 24 x 24 x 24 in. (including lid)
	Inner dimensions = 23.5 x 23.5 x 23.5 (excluding lid)
Heater	2 x 5 x 2 in. Experiment 1: 5.9 in. above ponded water line, centered laterally in salt Experiment 2: 2.0 in. above ponded water line
Salt height	19.2 in. above box floor
Ponded water	2.5 in. above box floor
Tracer injection port	2.8 in. above box floor, centered laterally in salt
Thermocouples	Bundle A = 1 in. from heater edge (narrow dimension) Bundle B = 3.25 in. from heater edge Bundle C = 6.75 in. from heater edge

Table 1. Dimensions and locations of apparatus in the salt laboratory experiments.

The experiment provided temperature data from the three thermocouple bundles and infrared camera images of the acrylic box faces; post-test moisture content data from destructive sampling; porosity data; and tracer gas breakthrough data. During Experiment 1, five breakthrough tests were successfully performed, two cool (pre- and post-test) injections and three injections during active heating. For Experiment 2 the pre-test injection and one heated injection were performed before the injection tube became clogged. Post-test forensics of the experiments during excavation of the salt provided information about zones of consolidation after heating.

The primary results of the experiments that relate to modeling efforts were the following:

- Although Experiment 2 had a cooler heater temperature than Experiment 1 by 60°C, the box sides were ~5°C warmer than Experiment 1 and the temperature gradient was considerably flatter. These results suggest heat pipe activity during Experiment 2.
- Porosity change was not distributed where pre-test modeling suggested it would be (Jordan et al., 2014).
- Porosity change is greatly accelerated by heating.
- Thermal data were a poor match to pre-test modeling with temperatures generally cooler than predicted.
- Gas breakthrough curves demonstrated clear evidence of porosity change and indicated its timing relative to heater initiation.

### 3.2 Model Setup

The grid was developed using LaGriT ([lagrit.lanl.gov](http://lagrit.lanl.gov)) with refinement down to minimum node spacing of 0.5 in. (1.3 cm) in the box (Figure 7). The mesh shown does not include the heater (dimensions 2 in. by 2 in. by 5 in.), the location of which varied between experiments and is shown in the subsections of section 3.3. Zones for the air outside the box, the air in the tank, the tank material, granular salt, heater, and bench were delineated. The ponded water, which affects

saturation in the granular salt but not granular salt material properties, is not shown. The properties of each zone are given in Table 2. The heater is not shown (its location varied between experiments; see Table 1). In Figure 7, the modeled domain is a quarter-space with reflection boundaries on the two faces shown in (b). The smallest node spacing is 1.27 cm.

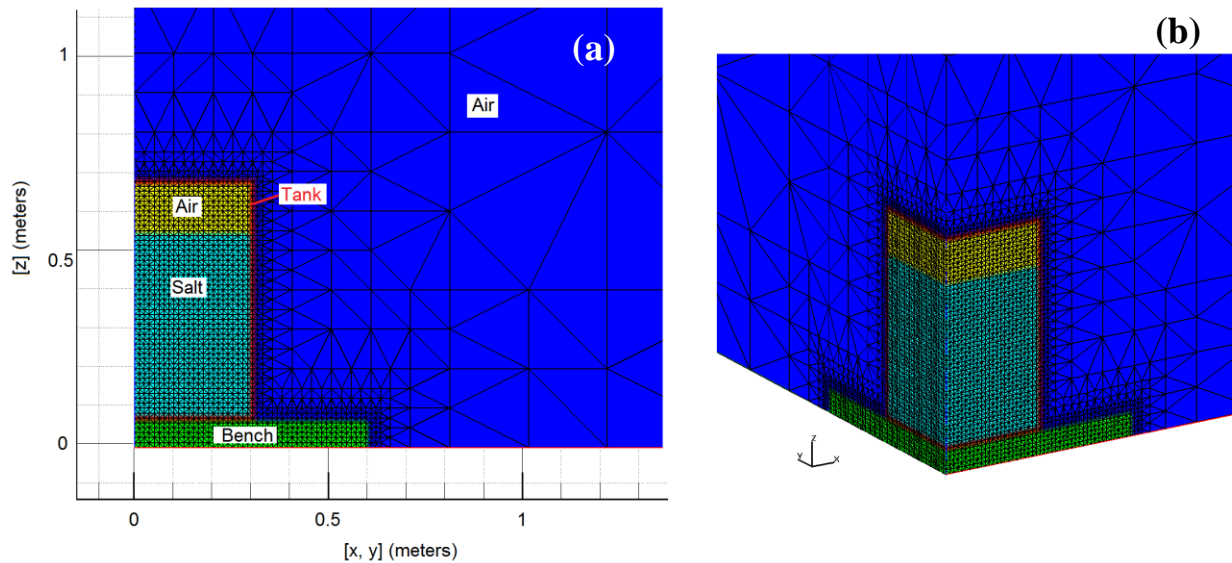


Figure 7. Zones in the numerical mesh used for modeling the laboratory experiment.

Transport in the model assumes the tracer undergoes temperature-dependent Henry's law partitioning. The free-air diffusion coefficient is modified by a tortuosity calculated using the Millington-Quirk model (Stauffer et al., 2013). Boundary conditions generally included no-flow boundaries at the far sides of the domain and a reflection boundary on the inner faces shown in Figure 7.

Parameter	Granular salt	Heater	Tank	Bench	Air
Solid density, kg/m <sup>3</sup>	2165	2230	2000	2000	-
Specific heat capacity,	931	710	1000	1000	0.46
Initial porosity	0.45	0.00001	0.00001	0.00001	0.999
Initial saturation	0.01, except ponded layer 0.99	1e-6	1e-6	1e-6	1e-6
Thermal conductivity, W/m-K	Variable (Stauffer et al., 2013)	1.1	1.05	1.05	14.0*
Permeability, m <sup>2</sup>	1e-12	1e-21	1e-25	1e-25	1e-8
Relative permeability model	Van Genuchten	Linear	Linear	Linear	Linear
Capillary suction model	Van Genuchten	Linear	Linear	Linear	Linear
Liquid residual saturation	0.01	0	0	0	1e-3
Maximum liquid saturation	1.0	1.0	1.0	1.0	1.0
Inverse of air entry head, 1/m	50**	-	-	-	-
Power <i>n</i> in Van Genuchten formula	4**	-	-	-	-
Maximum capillary pressure at zero saturation	0.2	0	0	0	1e-3
Tortuosity***	0.77	0	0	0	1

\* Based on a calculation for convective and radiative transfer in air, appropriate to in-drift disposal layout (Stauffer et al., 2013).

\*\* Based on a fit to Experiment 0 data (section 3.3.1).

\*\*\* Calculated based on Millington-Quirk (Stauffer et al., 2013); values given are for initial saturation and porosity, computed as  $\tau = (S_a n)^{7/3} / \phi^2$  where  $\phi$  is porosity and  $S_a$  is gas saturation.

Table 2. Simulation parameters for all modeled experiments.



### 3.3 Results

#### 3.3.1 Experiment 0

Useful results from this preliminary testing included the post-test water content profile and a tracer test with chloroform and no airflow. (All subsequent tracer tests during Experiments 1 and 2 were during active airflow.) The no-airflow boundary condition tracer test of Experiment 0 was modeled because it eliminates some of the uncertainty in the airflow modeling (e.g., accurate simulation of mixing in the headspace). Figure 8 shows the mesh for Experiment 0, with porosity shown to delineate the zones of differing materials. The salt is lower than in subsequent experiments, and the heater configuration is different. Initial and boundary conditions for the E0 model are given in Table 3. In Figure 8, different zones are shown by porosity (solid materials have  $n = 0.00001$ ; air is  $n = 0.999$ ; granular salt  $n = 0.45$ ; Table 2). The heater is situated in an upright position near the top of the salt (unlike in Experiments 1 and 2 where it lays horizontally closer to the bottom of the tank). Note that the heater was not activated before or during the E0 tracer test.

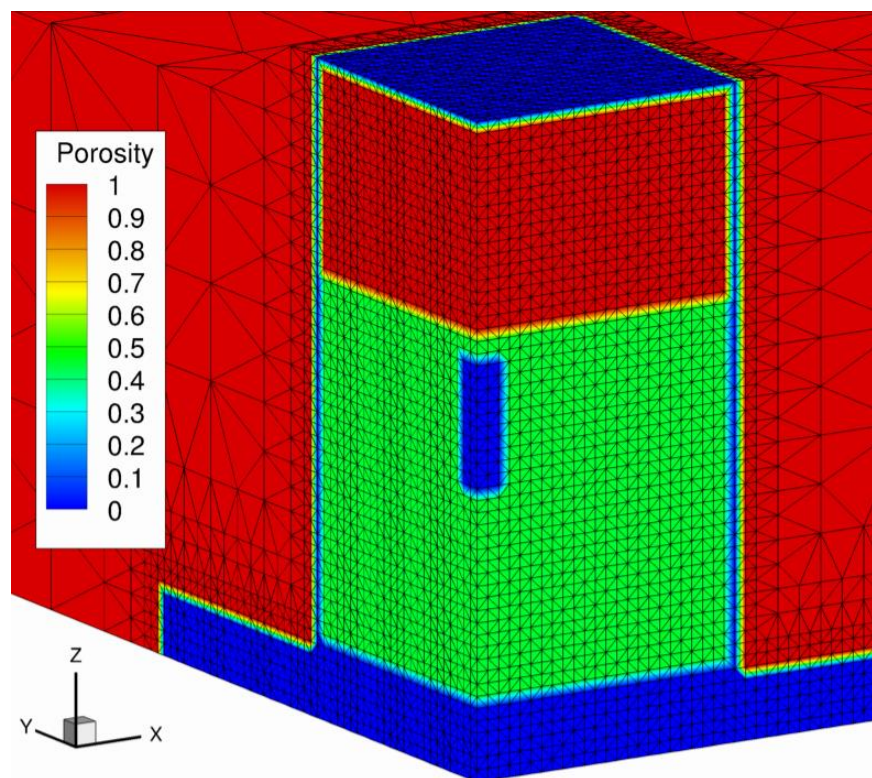


Figure 8. Numerical mesh for the model of Experiment 0.

Initial Conditions	
Temperature IC	23°C everywhere
Tracer IC	Based on 3 second injection simulation of 3.125e-4 mol
Boundary Conditions	
Temperature BC	23°C on back, right side, top, bottom faces
Flow/Tracer BC	No flow on back, right, top, bottom faces; reflection boundary on front, left sides

Table 3. Experiment 0 initial and boundary conditions.

### 3.3.1.1 Tracer results

The tracer test was performed before any heating but after the box had been sitting for ~2.5 months under various environmental conditions. The tracer was injected near the center of the box, ~5 cm from the bottom. Table 4 lists tracer amounts in this simulation. To accurately simulate injection by syringe, a simulation was first performed with slightly flowing air in one node to simulate 3 seconds of point injection (Figure 9). That the correct amount of tracer ( $3.125 \times 10^{-4}$  mol in the quarter-space) was injected was verified. In this experiment, 40 mL chloroform was injected as a gas by syringe.

Quantity	Chloroform	SF <sub>6</sub>
Total amount of tracer in domain, mol	$3.125 \times 10^{-4}$	N/A
Initial tracer concentration (injection)	31.5 mol/kg air	N/A

Table 4. Tracer information for E0.

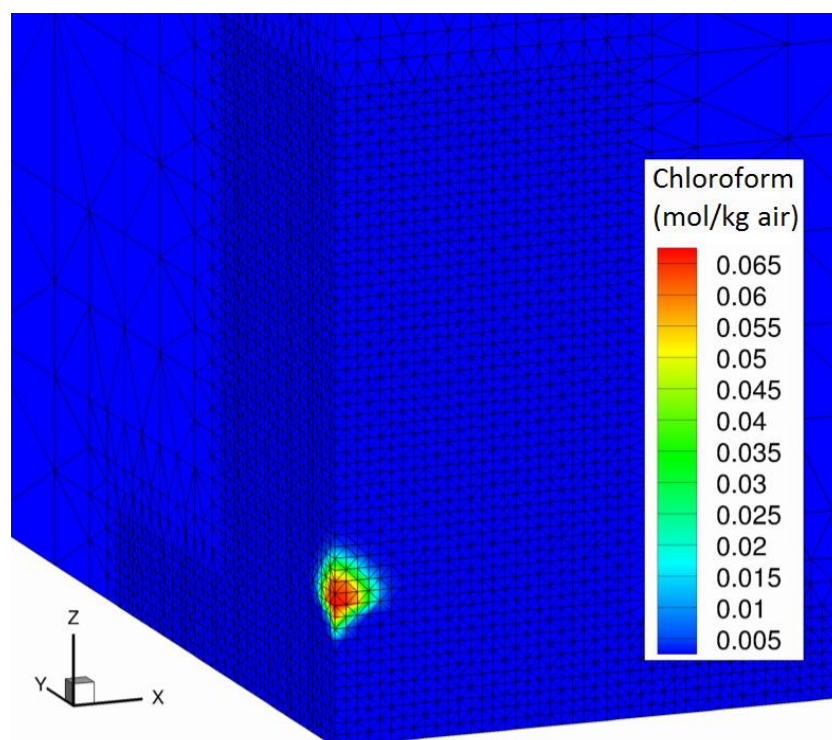


Figure 9. Simulated chloroform concentrations 3 seconds after injection.

Next, a simulation was restarted with the initial condition from the spread of tracer in the syringe injection simulation. The simulation ran for 1 day to model the unheated E0 chloroform tracer test for comparison with data.

The chloroform background concentration for the E0 data was estimated at 14.1 ppmv. At the end of data collection (~9 hours after injection), concentration of chloroform in the headspace was 17.3 ppmv. With background concentrations subtracted, this “equilibrium” value corresponds to  $1.1 \times 10^{-4}$  mol/kg air. At the same time in the simulation, airspace concentration

was  $4.7 \times 10^{-3}$  mol/kg air, a factor of ~40 times greater. The discrepancy between model and data for this experiment will be further investigated.

Due to the consistent shift in recovery between the data and simulations, all curves are shown normalized as  $C/C_{max}$  (as opposed to  $C/C_i$ , where initial concentration  $C_i$  was 31.5 mol/kg air) to compare the timing of breakthrough. The model had reached 92% of the equilibrium concentration by 9 hours; the data are normalized assuming  $C_{max}$  at 9 hours is 92% of the final maximum concentration. Figure 10 shows normalized data and breakthrough from the simulation. Using this scaling, the model/data match for breakthrough timing is excellent.

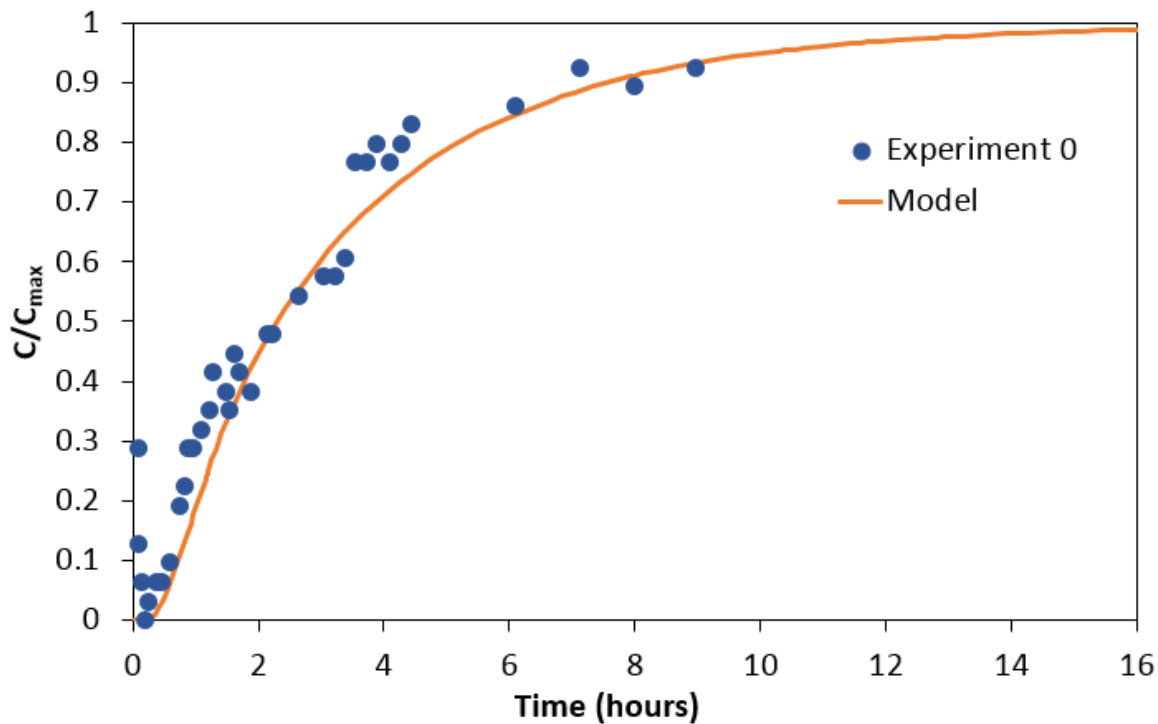


Figure 10. Experiment 0 tracer test data and model comparison.

The usefulness of the first chloroform tracer test in E0 is for comparison with water vapor migration data also collected during the same experiment (Jordan et al., 2015). While chloroform partitions into the liquid phase, it does not display hygroscopic behavior in salt like water vapor during migration.

### 3.3.1.2 Moisture Content/Suction

After three months of testing the salt box and equipment as part of E0, the salt was excavated and examined. Post-test forensics included thin section for porosity analysis and samples for moisture content (Jordan et al., 2015). The moisture samples were taken along a vertical line from the top of the salt to within the ponded layer. The samples were weighed, then oven-dried and reweighed. The moisture content in wt.% was converted to saturation by assuming the density in Table 2. The four samples sent for thin section analysis all had porosity of ~45%, but none of these samples were taken from the ponded layer. Assuming saturation of 1 in the ponded layer leads to porosity of 0.22 for that location. This may be reasonable, considering that

consolidation was observed at the bottom of the box. (A more complete porosity profile with depth, including the indurated layer, was taken for E1.) For comparison with model data, we assume the bottom sample had porosity of 0.22 and all other depths had porosity of 0.45. The experimental moisture content and model data are shown in Figure 11. The Van Genuchten parameters that produced the reasonable match shown were used for all models and are given in Table 2.

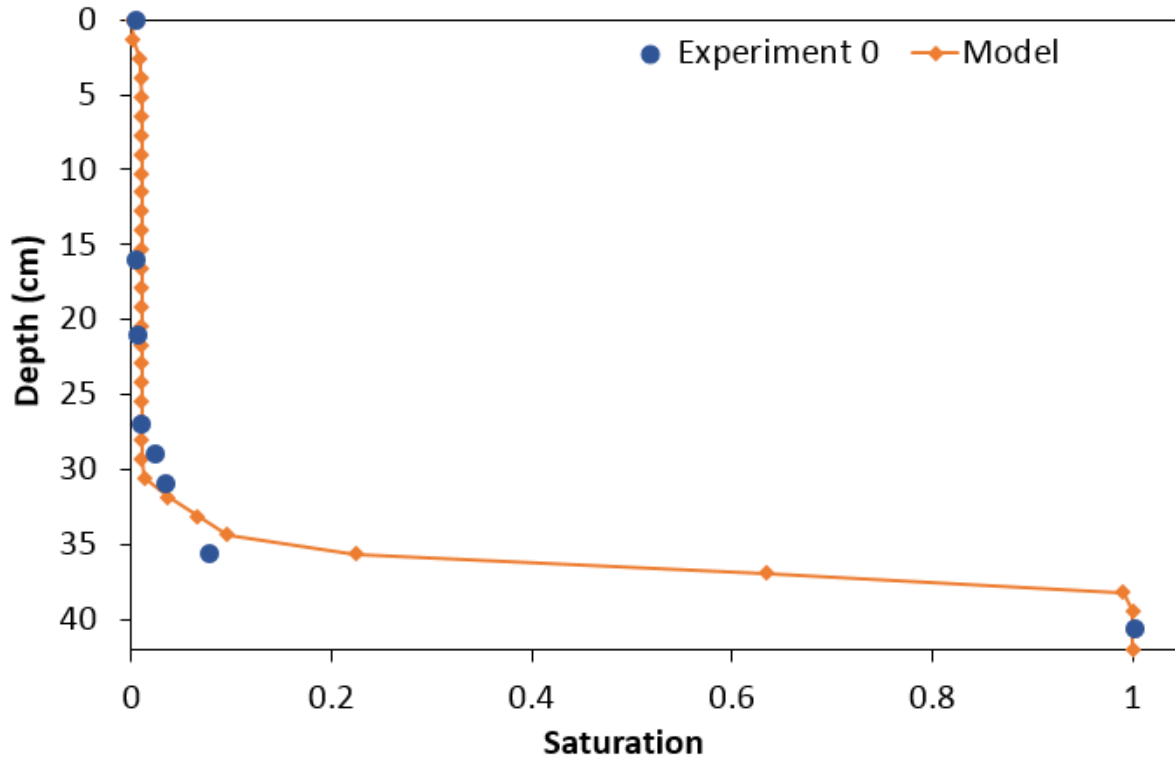


Figure 11. Saturation with depth in granular salt ( $t = 30$  days): Model vs data

Figure 12 shows saturation in the model domain at 30 days. Note that this experimental effort was not focused on determining retention characteristics, so we make use of the crude data and approximate fit shown here; uniform grain size granular salt is not the material of interest for a salt repository, so a dedicated effort to improve parameters for the granular salt model will not be performed. Individual process experiments on actual RoM salt in the future may be used for determining the parameters of interest to better accuracy for modeling drift-scale brine and water vapor transport around HGNW. Initially, saturation is 0.01 in the salt with the exception of the heater (zero saturation), while the ponded layer has saturation of 0.999.

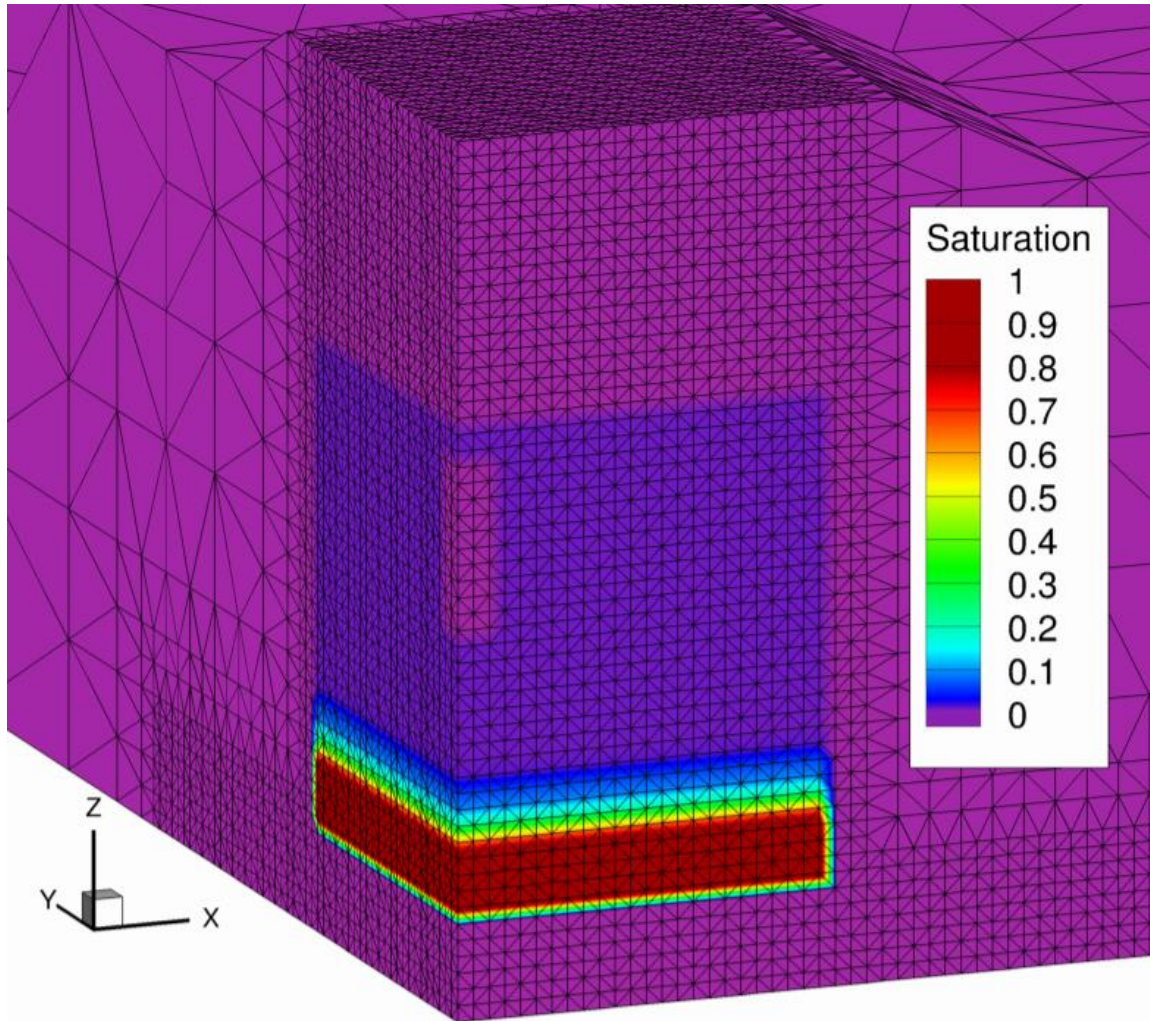


Figure 12. Saturation in the model after 30 days.

### 3.3.2 Experiment 1

Experiment 1 was the first and only experimental run with tracer data collected before, during, and after heating. All tracer tests were performed while airflow was active at 1.053 L/min (1.9 headspace turnovers per hour). Figure 13 shows the mesh for E1, with porosity shown to delineate the zones of differing materials. The salt is higher than in E0 and the heater is lower and oriented horizontally. Initial and boundary conditions for the E1 model are given in Table 5. In Figure 13 different zones are shown by porosity (solid materials have  $n = 0.00001$ ; air is  $n = 0.999$ ; granular salt  $n = 0.45$ ; Table 2). The mesh is cut away to show the top of the tank; air nodes above are hidden.

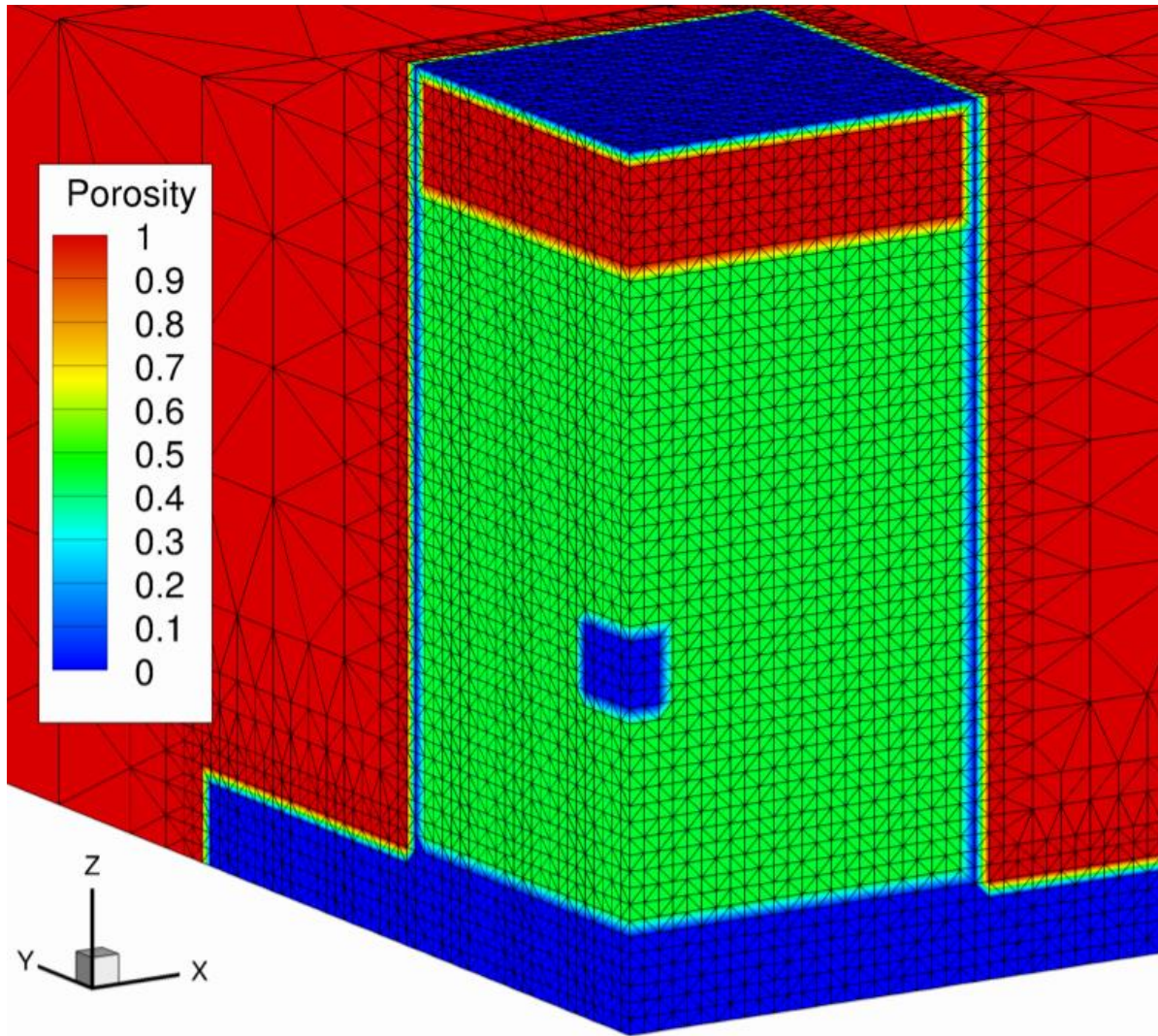


Figure 13. Numerical mesh for the model of Experiment 1.

Initial Conditions	
Temperature IC	23°C everywhere
Tracer IC	Based on 3 second injection simulation of 3.125e-4 mol
Boundary Conditions	
Temperature BC	23°C on back, right side, top, bottom faces Heater temperature 23°C to 260°C
Flow/Tracer BC	No flow on back, right, top, bottom faces; reflection boundary on front, left sides

Table 5. E1 initial and boundary conditions.

### 3.3.2.1 Tracer results

The first tracer test (T1) was performed before heating began (“cool”) on April 22, 2015. The next three tests (T2, T3, and T4) were performed during heating (“hot”). The final cool test (T5) was performed after temperatures at the thermocouple locations had stabilized. Chloroform was used during all tracer tests. The first three (T1-T3) used 0.1 mL chloroform only, vaporized to fill ~40 mL in a syringe. The final two tests (T4-T5) used a chloroform/SF<sub>6</sub> tracer mixture. All tracer data are presented in Jordan et al. (2015).

With the modifications to FEHM described above, the tracer runs from Experiment 1 with airflow can be modeled. Preliminary modeling with precipitation/dissolution of salt turned off was used to test the effects of airflow alone. Figure 14 shows chloroform tracer data from Experiment 1 with no heat (T1) and modeled (predicted) curves for different airflow rates. The airflow in the experiment was ~5e-6 kg/s, meaning that more analysis is needed to explain the experimental results.

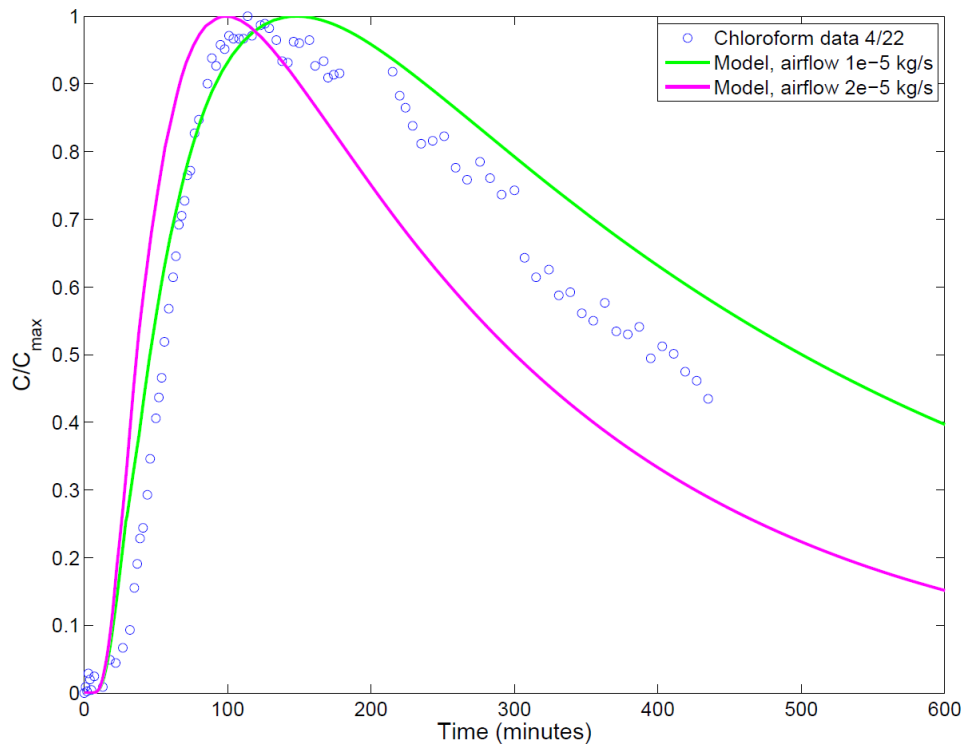


Figure 14. Chloroform data from Experiment 1, cool pre-test run (T1).

### 3.3.2.2 Thermal results

Observed temperatures for Experiment 1 were generally cooler than expected based on the numerical model (Figure 15), except near and within the ponded water layer. The numerical model uses the variable thermal conductivity functions of Stauffer et al. (2013). Additional research is necessary to determine the cause of the discrepancy.

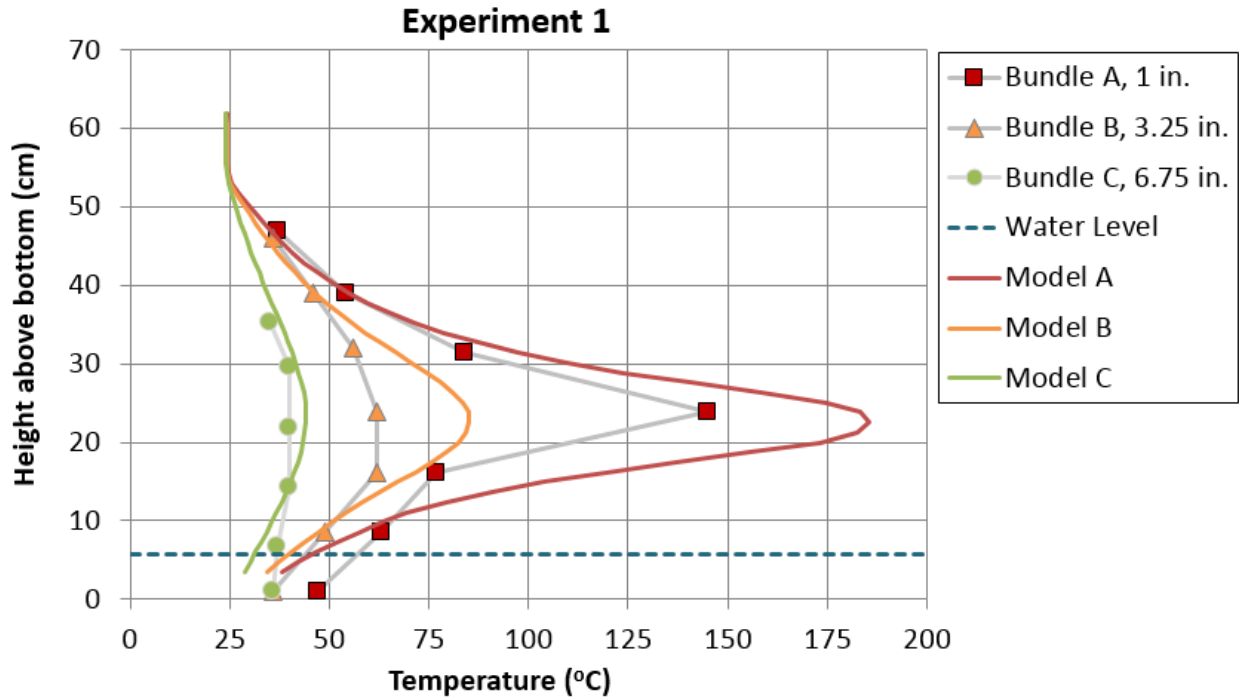


Figure 15. Temperature profile with depth for Experiment 1: Model vs Data

### 3.3.3 Experiment 2

In Experiment 2 the heater was closer to the water and maintained at a lower temperature (200°C). Airflow was slightly less than in Experiment 1, at 0.702 L/min (42,120 cm<sup>3</sup>/hr) and the headspace volume was greater, leading to a lower air turnover rate of approximately 0.65 cm<sup>3</sup>/hr. Figure 16 shows the numerical mesh for E2, with porosity shown to delineate the zones of differing materials. Initial and boundary conditions for the E2 model are given in Table 5. In Figure 16, different zones are shown by porosity (solid materials have  $n = 0.00001$ ; air is  $n = 0.999$ ; granular salt  $n = 0.45$ ; Table 2). The mesh is cut away to show the top of the tank.



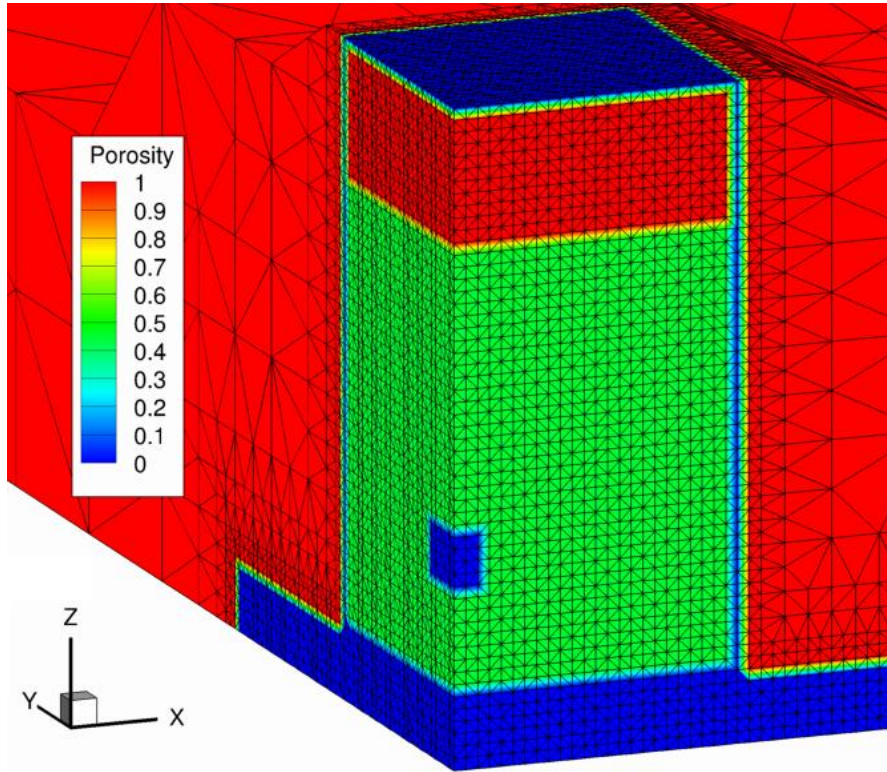


Figure 16. Numerical mesh for the model of Experiment 2.

Initial Conditions	
Temperature IC	23°C everywhere
Tracer IC	Based on 3 second injection simulation of $3.125e-4$ mol
Boundary Conditions	
Temperature BC	23°C on back, right side, top, bottom faces Heater temperature 23°C to 200°C
Flow/Tracer BC	No flow on back, right, top, bottom faces; reflection boundary on front, left sides

Table 6. E2 initial and boundary conditions.

### 3.3.3.1 Results

Numerical results from this experiment are ongoing and will be reported in fiscal year (FY) 2016.

#### 4. Heater Test Modeling

Design, fabrication and assembly of a full scale prototype heated canister began in May of 2014 and was completed by August 2014. Thermal testing began in October 2014 and continues (Sept 2015) in Carlsbad, NM. The stainless steel canister, initially obtained from LLNL in 2014, was designed to replicate a Savannah River National Laboratory defense high level waste canister (Figure 17).



Figure 17. Prototype canister heater.

The empty canister was cut open and a heating harness was installed (Figure 18). Next, ceramic beads with a thermal conductivity close to that of borosilicate glass was placed into the remaining void space within the canister. More details on the construction can be found in Stoller (2014). Maximum heating for both the primary and secondary variable load heater strip arrays is 1800W (Figure 19). Thermal measurements were made from thermocouples embedded within the canister, on the outside skin of the canister, and in the room air.



Figure 18. Heating harness inserted into canister.

A numerical representation of the canister was constructed using the LANL developed LaGrit ([lagrit.lanl.gov](http://lagrit.lanl.gov)) software. The numerical mesh is 1/4 of the experiment (Figure 17), and includes the canister, heater strips, ceramic fill, steel foot, cement floor, and air surrounding the canister (Figure 19). Reflections boundaries are shown on the upper right image in Figure 19.

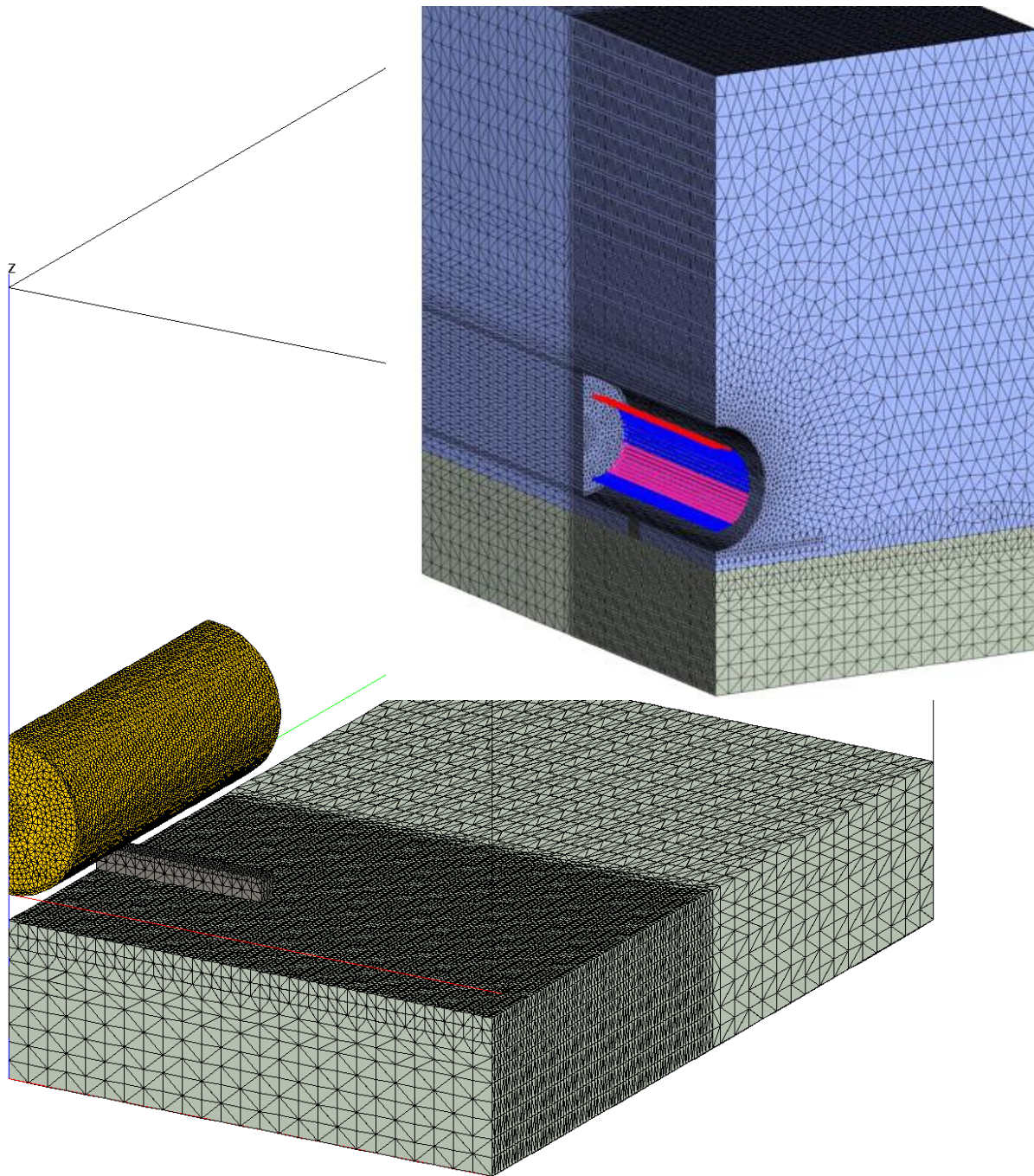


Figure 19. Numerical mesh of the prototype canister heater.

Canister testing was performed at the LANL Mobile Loading Building on Airport Ave in Carlsbad, NM. The heater was cycled at varying power levels from 250W to 1375W, and temperature data were recorded. Each cycle was run until the temperature curve began to asymptote to a near steady state (Figure 20).

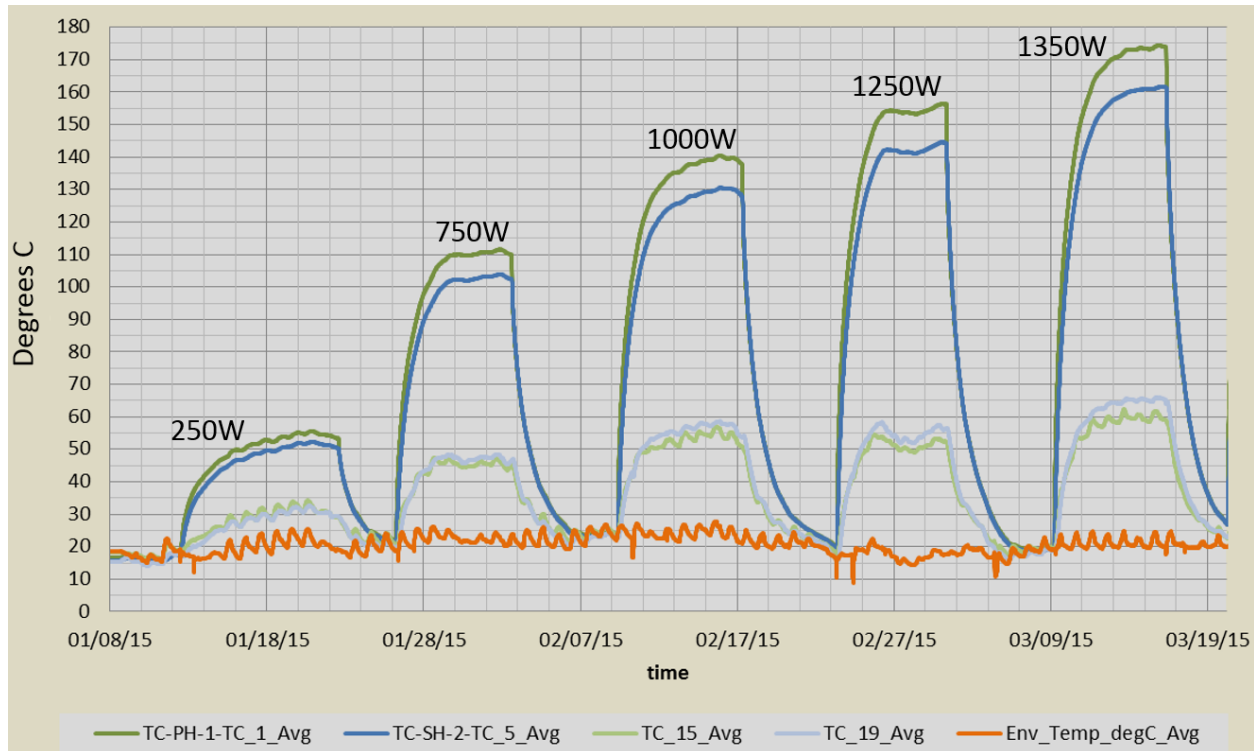


Figure 20. Temperature test data from the prototype canister.

Simulations using material properties based on readily available data for solid materials were fixed (cement, steel, and ceramic beads); however, the properties of air were allowed to vary to test different heat transfer conceptual models. Preliminary results reveal that the effective heat transfer across the steel/air boundary is best modeled by a low thermal conductivity skin coupled to a constant temperature air mass. Using values obtained from tuning the heat transfer at the boundary (one adjustable parameter) for a 250W experiment done in Oct. 2014, the simulations were able to obtain a relatively good match to the data at several monitoring points. The simulation was then re-run with a 1250W heat source and predictions were made in December 2014. Figure 21 shows these predictions relative to the 1250W test data from February 2015. Simulation data are generally in good agreement with the shape and approximate maximum temperatures. However, the simulations did not include variable air temperature and it is apparent from Figure 21 that the reduction in maximum temperature for the data is aligned with a period of low air temperature.

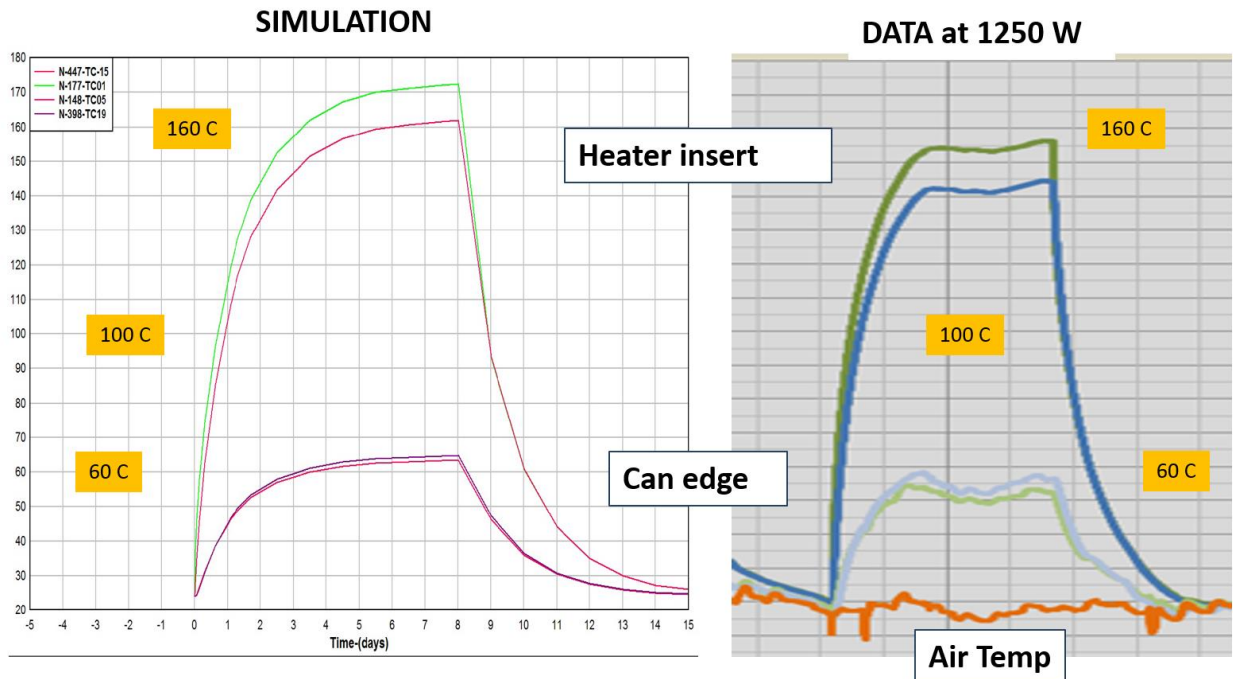


Figure 21. Temperature: Prediction vs Data for the 1250W prototype canister.

## 5. Hydrous Mineral Dehydration around Heat-Generating Nuclear Waste in Bedded Salt Formations (Published)

This section provides a copy of a journal publication accepted to ES&T in May 2015 that was funded through DOE-NE and includes model development components.

## Hydrous Mineral Dehydration Around Heat-Generating Nuclear Waste in Bedded Salt Formations

Amy B. Jordan,<sup>\*,†</sup> Hakim Boukhalfa,<sup>‡</sup> Florie A. Caporuscio,<sup>‡</sup> Bruce A. Robinson,<sup>§</sup> and Philip H. Stauffer<sup>†</sup>

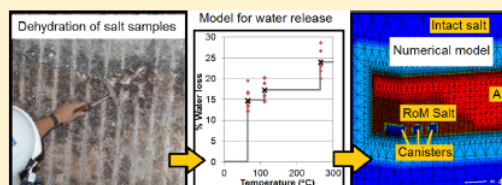
<sup>†</sup>EES-16: Computational Earth Science, MS T003, Los Alamos National Laboratory, Los Alamos, New Mexico 87545, United States

<sup>‡</sup>EES-14: Earth System Observations, MS J-599, Los Alamos National Laboratory, Los Alamos, New Mexico 87545, United States

<sup>§</sup>SPO-CNP: Civilian Nuclear Programs, MS H816, Los Alamos National Laboratory, Los Alamos, New Mexico 87545, United States

**S** Supporting Information

**ABSTRACT:** Heat-generating nuclear waste disposal in bedded salt during the first two years after waste emplacement is explored using numerical simulations tied to experiments of hydrous mineral dehydration. Heating impure salt samples to temperatures of 265 °C can release over 20% by mass of hydrous minerals as water. Three steps in a series of dehydration reactions are measured (65, 110, and 265 °C), and water loss associated with each step is averaged from experimental data into a water source model. Simulations using this dehydration model are used to predict temperature, moisture, and porosity after heating by 750-W waste canisters, assuming hydrous mineral mass fractions from 0 to 10%. The formation of a three-phase heat pipe (with counter-circulation of vapor and brine) occurs as water vapor is driven away from the heat source, condenses, and flows back toward the heat source, leading to changes in porosity, permeability, temperature, saturation, and thermal conductivity of the backfill salt surrounding the waste canisters. Heat pipe formation depends on temperature, moisture availability, and mobility. In certain cases, dehydration of hydrous minerals provides sufficient extra moisture to push the system into a sustained heat pipe, where simulations neglecting this process do not.



### INTRODUCTION

The question of where to store the nation's heat-generating nuclear waste (HGNW) provides motivation for scientific research on disposal options. HGNW is composed of both high-level nuclear waste (HLW) from nuclear weapons production and spent nuclear fuel (SNF) from civilian and defense reactors. A number of potential geologic media have been proposed for HGNW repositories, including volcanic tuff, shale, clay, crystalline rock, and both bedded and domal salt.<sup>1–3</sup>

Multiple geologically stable salt formations in the U.S. may be suitable for nuclear waste disposal.<sup>1</sup> Salt has unique temperature-dependent viscoplastic properties that contribute to self-sealing of tunnels and other disturbed zones to low permeabilities associated with intact salt<sup>4</sup> in relatively short time periods (tens to hundreds of years);<sup>1,5</sup> it also has a high thermal conductivity when intact or reconsolidated; and salt is relatively easy to mine. These characteristics make salt a favorable option for locating a nuclear waste repository.<sup>1</sup> Long-term performance of a potential HGNW repository in salt will be dominated by the mechanical deformation of salt surrounding the waste, which will ultimately lead to room closure of the drifts and isolation of the waste canisters in low-permeability intact salt, but physical and chemical processes functioning around the HGNW in the first few years have implications for extended repository evolution.<sup>1,6</sup>

Domal salt formations are being extensively studied for nuclear waste storage in Germany<sup>7,8</sup> and in the United States

for HGNW and natural gas storage.<sup>7,9</sup> Bedded salt has been studied at the Waste Isolation Pilot Plant (WIPP) in southern New Mexico, and elsewhere in the U.S.<sup>7</sup> Recently, a new “in-drift” waste emplacement strategy for disposal of HGNW has been proposed.<sup>10</sup> In this method, waste canisters are placed directly on the floor of horizontal drifts, and run-of-mine (RoM) excavated material is used as backfill over them (Figure 1). In the configuration used for this study, RoM salt fills the drift to the back, to both sides, and leaves an air gap between the top of the backfill and the roof of the drift. Bedded salt is far more heterogeneous and contains a higher mass fraction of hydrous minerals, such as clay and gypsum, than domal salt.<sup>11</sup> Thus, in-drift disposal in bedded salt will result in hydrous minerals being incorporated into the RoM salt backfill.

Clays in bedded salt may be present both in relatively pure layers up to several cm thick, or finely dispersed.<sup>4,12</sup> The temperature, timing, and amount of water released from clay dehydration depends on the presence of electrolytes, relative humidity, temperature, and pressure.<sup>13</sup> Sulfate minerals are also identified in WIPP samples, such as gypsum ( $\text{CaSO}_4 \cdot 2\text{H}_2\text{O}$ ), anhydrite ( $\text{CaSO}_4$ ), and polyhalite ( $\text{K}_2\text{Ca}_2\text{Mg}(\text{SO}_4)_4 \cdot 2\text{H}_2\text{O}$ ). Gypsum (21 wt % water) can transition directly to anhydrite or

Received: February 25, 2015

Revised: May 9, 2015

Accepted: May 12, 2015

Published: May 12, 2015

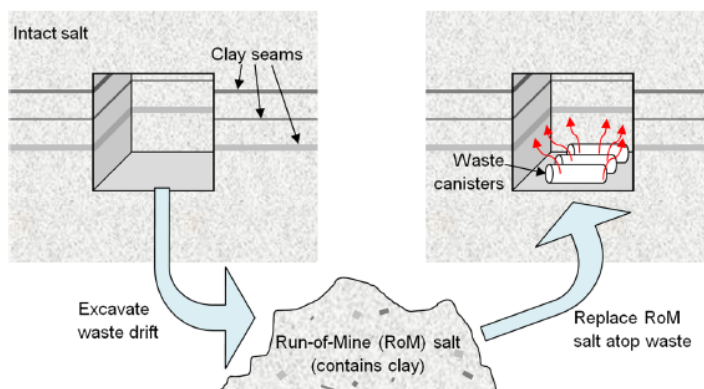


Figure 1. Schematic of the in-drift waste disposal concept.

to metastable bassanite ( $\text{CaSO}_4 \cdot 0.5\text{H}_2\text{O}$ ), followed by a bassanite to anhydrite transition. Other hydrous minerals that may be present include camallite ( $\text{KMgCl}_3 \cdot 6\text{H}_2\text{O}$ ), kieserite ( $\text{MgSO}_4 \cdot \text{H}_2\text{O}$ ), and bischofite ( $\text{MgCl}_2 \cdot 6\text{H}_2\text{O}$ ).<sup>14</sup> Temperatures for dehydration transitions have been measured for several scenarios by previous authors, with varying results.<sup>13–16</sup>

Heating at the base of a high-permeability pile of RoM salt leads to natural convection and the creation of a chimney with hot air rising above the waste packages. If there is sufficient mobile water and heat supplied by the waste, a three-phase heat pipe may form in the RoM salt. In a heat pipe, liquid water is vaporized in a boiling region, convects and diffuses along vapor concentration gradients to cooler regions where it recondenses and flows back toward the heat source by a combination of gravity flow and capillary pressure gradients.<sup>17,18</sup> If brine re-enters the boiling region, it will vaporize and deposit dissolved salt as a precipitate, contributing to the buildup of a low-porosity rind around the waste.

Bench-scale laboratory investigations have produced heat pipes in moist salt under relevant repository conditions.<sup>19</sup> One component of the heat pipe process has been observed in situ at WIPP: deposition of low-porosity salt during boiling of brine.<sup>20</sup> Numerical simulations of in-drift disposal of HGWN show that if a heat pipe forms, the process can cause significant changes in the time evolution of temperature, saturation, and porosity of the backfilled RoM salt around the waste in the first few years after waste disposal.<sup>21</sup>

Numerical modeling of HGWN disposal in salt has been performed by multiple groups for WIPP and for other salt repositories worldwide,<sup>7</sup> but simulation of the strongly coupled thermal, hydrological, mechanical, and chemical (THMC) processes have been done only at small spatial scales.<sup>22</sup> Current state-of-the-art simulators for repository-scale simulations have been limited to incomplete coupling, e.g., only simultaneous coupling of THM processes to capture the viscoplastic reconsolidation behavior of salt, or only coupled THC processes to include the effects of porosity change from precipitation and dissolution across temperature gradients.<sup>21,23–26</sup> The THC model developed here does not include mechanical effects that lead to room closure and RoM reconsolidation. However, the modeled THC processes operating on short time scales may be important to the salt repository safety case because of impacts including different rates of reconsolidation of RoM backfill based on moisture

content,<sup>5,27</sup> altered potential for corrosion of the waste canisters, gas generation, and a modified thermal regime (e.g., maximum temperatures reached) immediately surrounding the waste.

Initial coupled THC simulations indicated that the amount and mobility of water in the RoM backfill would play an important role in governing whether an active heat pipe would form.<sup>21</sup> Considerable uncertainty exists in the amount, production, and retention characteristics of water in bedded salt formations.<sup>14</sup> Water in the system is found as fluid inclusions in salt crystals, within the boundaries between salt grains, or associated with hydrous minerals. The mobility of these different populations of water, their chemical composition, and their relative amounts vary significantly within bedded salt. Among these different water populations, water associated with hydrous minerals may represent a substantial fraction of moisture contained in salt.<sup>15</sup> This paper presents a synthesis of ongoing model development research<sup>21</sup> related to the impact of water-producing physicochemical processes caused by the heating of hydrous minerals. Our research advances prior HGWN models for bedded salt and presents an example that shows the potential importance of including mineral dehydration in salt repository calculations.

The goal of this study is to incorporate a new empirically derived hydrous mineral dehydration model for bedded salt into a state-of-the-art coupled numerical simulator to predict the impact of available moisture on fluid and heat transport. In the following sections, we first present recent experimental hydrous mineral dehydration data from bedded salt samples. Next, these data are used to develop a simple model for hydrous mineral water releases as a function of temperature. This model is then implemented into a numerical porous flow simulator. Simulations are run for 2 years of heating by HGWN canisters emplaced using the in-drift disposal method. Because of large uncertainties in flow properties, hydrous mineral mass fraction, and initial water content of RoM salt, many simulations were performed across parameter space. We present a subset of these simulations that highlights the importance of including the hydrous mineral water source.

## ■ MATERIALS AND METHODS

**Salt Sampling and Characterization.** Thirteen RoM salt samples (100–200 g) were collected from WIPP, which is mined in a bedded Permian-age salt formation 650 m below the

surface, that represented a range of impurity content and mass fractions in the salt, including mapped units such as clay seam F, the orange marker bed, and relatively pure halite from the drift floor in a freshly excavated room.<sup>4,15</sup> The samples were sealed in plastic bags using an impulse heater immediately after exiting the underground mine, and were kept in a sealed, large plastic container until utilized. Residual minerals from the samples were analyzed by X-ray diffraction (XRD). Residues from clay seam F and orange marker bed samples were composed primarily of corrensite— $(\text{Mg,Fe,Al})_9((\text{Si,Al})_8\text{O}_{20})(\text{OH})_{10}\cdot 4\text{H}_2\text{O}$ —with minor amounts of quartz, magnesite, mica, kaolinite (or possibly chlorite), hematite, and anhydrite. All samples contained halite.

**Gravimetric Characterization of Salt Dehydration.** The bulk samples (100–200 g) were weighed at the start of the experiment, heated to certain designated temperatures, and weighed again every 8–12 h until the weight stabilized (typically, within 24–72 h). Once a constant weight was achieved at the first temperature, the sample was heated to the next desired temperature and the process was repeated. The temperatures were 65, 110, 165, and 265 °C. These temperatures were chosen based on expected dehydration reactions. A portion of the samples were removed from the heaters after 65 and 110 °C and allowed to rehydrate. The maximum vacuum applied was 15 mmHg at 265 °C to ensure the release of all water associated with the rock salt. The moisture released from these experiments was not collected.

**Thermogravimetric Analysis of Salt and Accessory Minerals.** Thermogravimetric analyses (TGA) of natural clay-rich samples and washed clay samples were obtained using a TA Instrument Inc. Q500 coupled with a mass spectrometer that allows resolution of ion masses  $\pm 1.0$  amu. The instrument was operated by equilibrating the samples at room temperature for 2.0 min followed by a constant temperature ramp of 5 °C/min from room temperature to 350 °C. The instrument was operated under a constant 40 mL/min flow of high-purity nitrogen. All experiments were performed on clay specimens of 1.5–2.0 mg collected from WIPP salt samples obtained from clay seam F. A fraction of the gas flow through the sample was continuously run through the mass spectrometer, allowing characterization of the ion masses of the substances released from the sample as a function of temperature.

**Numerical Model.** The porous media flow and transport simulator FEHM was used to explore the impacts of mineral dehydration on mass transfer for an in-drift repository-scale example. FEHM uses the control volume finite element method to solve the governing equations of mass and momentum conservation, assuming a multiphase form of Darcy's Law is valid for all phases across the domain, and includes advection, diffusion, and phase changes.<sup>28</sup> Many new capabilities have been added to FEHM to model the tightly coupled THC processes of fluid transport in heated salt in the RoM backfill and DRZ, including the following:<sup>21</sup> porosity change from precipitation/dissolution of salt; salt solubility increasing with temperature; permeability increasing with porosity using a power law model with experimentally derived coefficients;<sup>29</sup> thermal conductivity of salt as an empirical function of porosity and temperature;<sup>25</sup> vapor pressure of water as an empirical function of concentration and temperature;<sup>30</sup> and water vapor diffusion as a function of saturation, porosity, pressure, and temperature. The Millington–Quirk approach<sup>31</sup> is used to calculate the tortuosity ( $\tau$ ), which modifies vapor-phase free-air diffusivity based on air saturation ( $S_a$ ) and porosity ( $\phi$ ), by

$$\tau = (S_a\phi)^{7/3} / \phi^2 \quad (1)$$

A hydrous mineral dehydration model based on our experimental results was developed and used in numerical simulations of a drift in a HGNW repository. Five heated waste canisters, each a fixed enthalpy source of 750 W, 0.3-m radius, and 2.4-m length, were spaced 0.3 m apart on the floor of a 4.9 m wide by 3.0 m high drift. Salt backfill over the canisters extended 1.8 m in height above the drift floor, to the sides of the drift (4.9 m), and 8.5 m in length at the bottom, tapering toward the top (total volume of RoM salt: 57 m<sup>3</sup>). A section of the numerical mesh developed for simulations of this experiment is shown in Figure 2. The model represents a

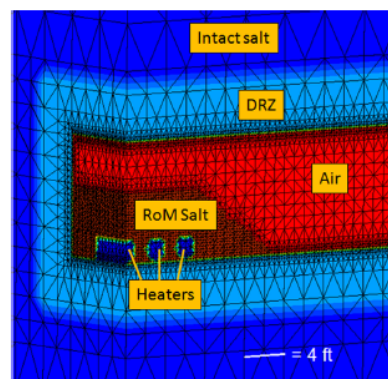


Figure 2. Numerical mesh showing the zones of the model: intact salt, damaged rock zone (DRZ), air, run-of-mine (RoM) backfill, and the heated waste canisters.

quarter space, with reflection boundaries on both faces seen in Figure 2. The zones represent the undisturbed, intact salt of the repository; the damaged rock zone (DRZ) with enhanced permeability due to damage related to excavating the drift; air; the RoM salt backfill; and the heated waste canisters.

The DRZ permeability was initially  $10^{-19}$  m<sup>2</sup>, while the intact salt permeability was  $10^{-21}$  m<sup>2</sup>. This model, which was used for short-term calculations, does not include any mechanical deformation of salt. Following excavation of the drifts, the permeability of the DRZ is expected to evolve anisotropically due to fracture healing and viscoplastic creep that eventually leads to room closure;<sup>4</sup> in the current work, permeability change in the DRZ is only caused by salt precipitation and dissolution. RoM backfill reconsolidation may affect the porosity structure and have important feedbacks on hydrological parameters, as investigated by multiple experiments and TM and THM models.<sup>5,23,24,32</sup>

The RoM backfill was modeled to contain accessory hydrous minerals. The typical accessory mineral content ( $f_i$ ) in bedded salt formations is highly variable, ranging from very little (<1 wt % for nearly pure halite)<sup>1</sup> to argillaceous halite (up to 5 wt %),<sup>12</sup> with even higher amounts (up to 16 wt % in our samples) found in the thin clay seams and marker beds.<sup>12,14,15</sup>

The simulations are performed in volumetric saturation space, with initial volumetric saturations ( $S_i$ ) varying from 0.01 to 0.07 (1–7%), while the experimental data are presented in water mass fraction units (mass of water/mass of sample). At a porosity of 0.35 and salt density of 2165 kg/m<sup>3</sup>, volumetric saturation of 1% corresponds to mass fraction of 0.25 wt %, and



7% volumetric saturation is 1.8 wt %. Maximum capillary suction ( $P_{c,max}$ ) at residual saturation and  $S_i$  are highly uncertain and are varied in our simulations. The parameters used in the simulations discussed in the main text and Supporting Information (SI) are shown in Table 1. Values of  $P_{c,max}$  greater

Table 1. Simulation Parameters

		$f_c$ (%)	$S_i$ (%)	$P_{c,max}$ (MPa)
case 1	(a)	0	1	0.2
	(b)	10	1	0.2
case 2	(a)	0	7	1.0
	(b)	10	7	1.0
case 3	(a)	10	1	0.2
	(b)	10	1	1.0
case 4 (SI)	(a)	0	5	0.2
	(b)	0	10	0.2
	(c)	0	10	1.0

than those observed<sup>29</sup> are included because of uncertainty in the grain size distribution in RoM salt as well as extrapolation to very low saturation (e.g., in the boiling front very near the canisters). An inverse linear relationship between capillary suction and saturation was used due to large uncertainties in the retention characteristics of mixed-grain size, consolidating RoM salt under conditions of changing porosity.<sup>21,29</sup>

## RESULTS AND DISCUSSION

**Moisture Release from Run-of-Mine Salt as a Function of Temperature.** In the dehydration experiment, an initial weight gain ranging from 0.1–0.8 wt % occurred for all samples, which was due to moisture absorption during equilibration of samples at room temperature before the start of the dehydration experiment. Heating clay-rich salt samples to 65 °C resulted in total sample weight loss of 1.2–2.1 wt %. By fraction of clay and other accessory minerals, the loss was 12.1–19.6% of hydrous mineral mass (average 14.8%) at 65 °C. Clear salt samples, which contained very small amounts of accessory minerals, lost less than 0.25 wt % of their total weight at 65 °C. Dehydration of the clay rich samples at 65 °C was reversible; 3 samples removed from the oven and placed in a moist chamber recovered their weight and then continued to accumulate water rapidly.

The clay-rich samples heated to 110 °C lost 1.3–2.5 wt %. By hydrous mineral fraction this was 14.6–20.4% of clay mass, with an average of 17.3% (or 2.5% additional mass loss from dehydration following the water loss at 65 °C). Clear salt with minimal accessory minerals had water loss of less than 0.06 wt %.

At 165 °C, the samples lost no additional weight after heating for 15 h. The dehydration process was still reversible; a subset of samples removed from the experiment to a moist environment rapidly recovered all the moisture lost and then accumulated additional moisture due to the abundance of clay in the samples, which can undergo rapid and reversible hydration/dehydration processes, and water sorption onto the surface of both the clay and RoM salt grains.

The temperature was raised to 265 °C for the final test of water loss. Samples lost a total of 0.09–3.5 wt %, or 20.1–28.7% of hydrous mineral mass (average of 24.0%, or 6.7% more following the previous dehydration to 110 °C).

The total weight loss is correlated with samples' accessory minerals content, rejecting the hypothesis that the water

released upon heating is primarily intergranular pore fluid or intragranular brine inclusions for the clay-rich samples. Furthermore, the reversible water loss for  $T < 110$  °C is consistent with temperatures under which corrensite undergoes hydration/dehydration processes: the XRD and TGA results provide strong evidence of loss of interlayer water (5–13 wt %) at 65–75 °C.<sup>15</sup> Concurrently, at around 75 °C, the gypsum to bassanite phase transformation can release up to 15 wt % water. The cause of the water loss at higher temperatures may be from further dehydration of both mineral groups, particularly bassanite to anhydrite, which can release an additional 6 wt % water.

TGA experimental and mass spectrometer data are shown in Figure 3, showing the weight loss and heat flow recorded

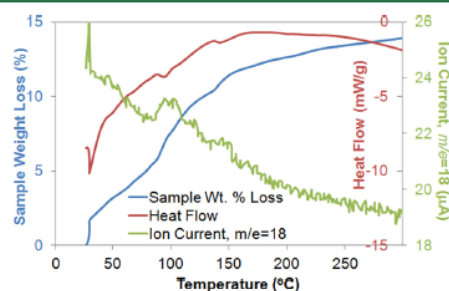


Figure 3. Dehydration of accessory minerals from a sample obtained from clay seam F at WIPP. The blue line shows the weight loss as a function of temperature, the red line indicates the heat flow during dehydration, and the green line indicates the ion current for  $m/e = 18$ .

during the dehydration of a clay-rich sample, along with the ion current for mass to charge ratio ( $m/e$ ) of 18 (water). The data show an increase in the ion current indicating an initial water release, additional water release just below 50 °C and slightly above 50 °C, between 90 and 100 °C, and between 140 and 170 °C. The weight loss and energy flow curves show significant changes in the same temperature domains, with decreases in heat flow during mass loss indicating endothermic processes. Similar experiments performed on clay samples that have been washed repeatedly to eliminate any soluble minerals show a more pronounced weight loss between 50 and 70 °C and lose the features visible between 90 and 100 °C and between 140 and 170 °C (SI Figure S1). The weight loss observed at 50 °C is most likely from water absorbed to mineral grain surfaces, primarily clays. The second weight loss (70 °C) is coincident with dehydration experiments of corrensite clay from previous experiments,<sup>15</sup> along with the transition of gypsum to bassanite. The third weight loss, occurring near 100 °C, is most likely due to initial phase transformation of bassanite to anhydrite.<sup>33</sup> The water loss at 150 °C may also be due to the bassanite to anhydrite phase transformation, which is kinetically driven and may occur in stages. Alternatively, the water loss at 150 °C may be due to another mineral breakdown (such as  $MgCl_2$ ) which undergoes several dehydration stages, one of which occurs between 140 and 170 °C. Polyhalite loses its hydrate water at temperatures above 250 °C, and can lose up to 6 wt % as water. Carnallite, kieserite, and bischofite may also contribute to water loss of RoM samples under heating.<sup>15</sup> Above 250 °C, water loss may be contributed from intragranular fluid inclusion release due to decrepitation.<sup>34</sup> Although the measured weight loss curves are highly useful for

developing a water source term model, additional experimental characterization of the clay composition and the dehydration of the different species is needed to confirm the processes producing the temperature-dependent weight loss curves.

**Numerical Dehydration Model.** Averages of the water loss data as a function of temperature from the bulk salt samples were used to develop a hydrous mineral dehydration water release model (Figure 4).<sup>21</sup> The model uses a simple

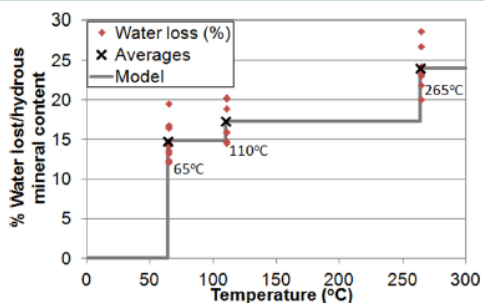


Figure 4. Weight lost as a percentage of hydrous mineral weight during the heating experiment and the stepwise dehydration model.<sup>21</sup>

stair-step function, and does not allow rehydration. Because temperatures monotonically increase and remain elevated in the backfill salt around the waste for the short-term (<2 years) duration of these model runs, rehydration is not expected. Representing hydrous mineral dehydration as one-time releases is a simplification of kinetically driven water release as a function of temperature, justified by uncertainty due to heterogeneity in hydrous mineral quantities and relative abundances in a repository setting, and with the caveat that this dehydration model is used only to demonstrate order-of-magnitude effects that may be of importance to the repository safety case.

As implemented in FEHM, the hydrous mineral dehydration model can be applied to selected nodes or zones within the model, and differing mass fractions of hydrous mineral content can be specified across the model, e.g., if clay seams are explicitly modeled. On the basis of the averaged experimental data discussed above, at 65 °C, 14.8% of the mass of hydrous minerals in the node is added as a source term in a one-time release. At 110 °C, an additional percentage is released as water (2.5%), and at 265 °C, more water is released (6.7%) for a total mass release of 24.0% of the hydrous mineral weight. For a given node for which the dehydration model is invoked, for a specified mineral mass fraction  $f_c$ , the mass of water produced for the first 65 °C dehydration is given by

$$M_w = f_1 f_c (1 - \phi_i) \rho_c V_{\text{cell}} \quad (2)$$

where  $f_1$  is the fractional weight in water released at the first dehydration (0.148),  $\phi_i$  is the initial porosity of the node,  $\rho_c$  is the density of clay, and  $V_{\text{cell}}$  is the volume of the node. The water mass production for the second and third dehydration temperatures follows similarly, with  $f_2 = 0.025$  and  $f_3 = 0.067$  replacing  $f_1$  in eq 2 (Figure 4). The release of pure water from mineral dehydration causes dissolution of solid salt and a corresponding change in porosity.<sup>21</sup> The implementation of the new hydrous mineral dehydration model in FEHM was tested in a simplified 6-node simulation and it compared closely to calculated values.<sup>21</sup>

**Numerical Model Results.** For a Case 1b, Figure 5 shows the porosity and temperature at 460 days. The initial porosity

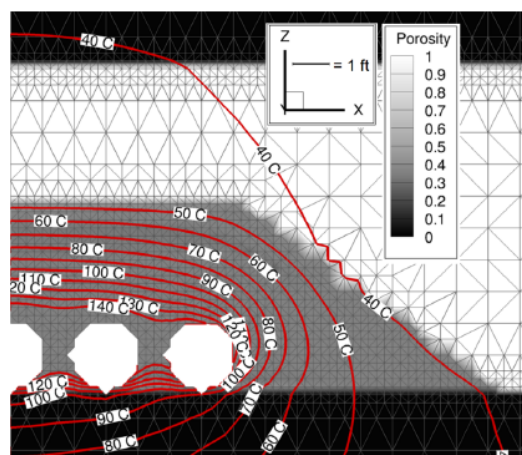


Figure 5. Porosity and temperature around the heaters at 460 days for a case with  $f_c = 10\%$  in the RoM salt. RoM  $\phi_i = 0.35$ ,  $S_i = 1\%$ , and  $P_{c,\text{max}} = 0.2$  MPa (Case 1b).

in the DRZ above and below the drift is 0.01, porosity in the air is 0.999, and initial porosity in the RoM salt pile, where significant precipitation and dissolution would be expected if a heat pipe were to form, is  $\phi_i = 0.35$ . After 460 days of heating, however, the porosity is not significantly changed from the initial state, in this case. This indicates very little heat pipe activity.

The saturation, porosity, and temperature differences at 460 days between 10% clay and the corresponding simulation with no clay are shown in Figure 6. Only minor differences are observed in this example in the temperature and porosity. That is, the dehydration process has only a minor impact on the final state of the system in Case 1.

In Figure 6c, a ring of higher saturation persists outside the boiling region for the hydrous mineral-bearing case. The core of the RoM salt is also cooler because of latent heat transfer. The total amount of water produced in the simulation with 10% hydrous minerals in the RoM salt pile in the model (one-quarter of the full salt pile) is 119 kg at 460 days. By comparison, the total initial amount of water in the RoM salt with  $S_i = 0.01$  and porosity 0.35 is 50.4 kg.

The preceding example is a case where hydrous mineral dehydration causes only small changes in the final temperature and porosities observed after 460 days of heating. Case 2 shows that the presence of hydrous minerals can cause major differences, with evidence for heat pipe activity when dehydration releases additional water (Figure 7). Evidence for heat pipe activity includes lower porosity around the heaters from evaporating brine, a high-porosity region where water vapor condenses and dissolves the RoM solids, and a flatter temperature gradient around the canisters<sup>35</sup> (Figure 7b). Differences in temperature and porosity at 460 days are shown in Figure 8 for simulations with and without hydrous mineral dehydration. This time, the difference in final temperature (Figure 8a) is significant, with heater temperatures up to 25 °C cooler. The heat pipe efficiently transports heat

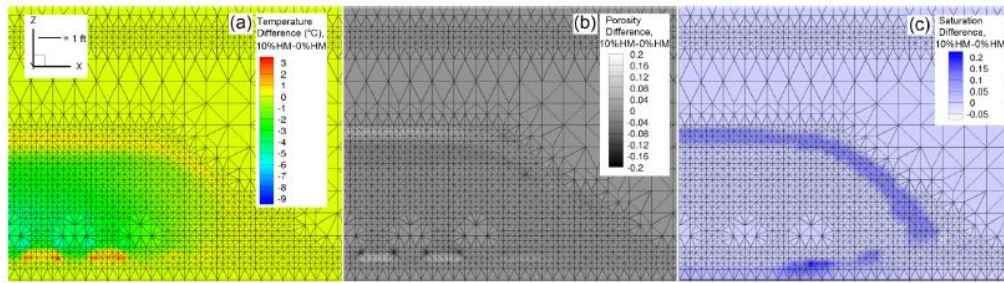


Figure 6. Differences of  $f_c = 10\%$  (Case 1b) minus pure halite ( $f_c = 0\%$ , Case 1a) at 460 days with  $S_i = 1$  and  $P_{c,max} = 0.2$  MPa: (a) temperature, (b) porosity, and (c) saturation.

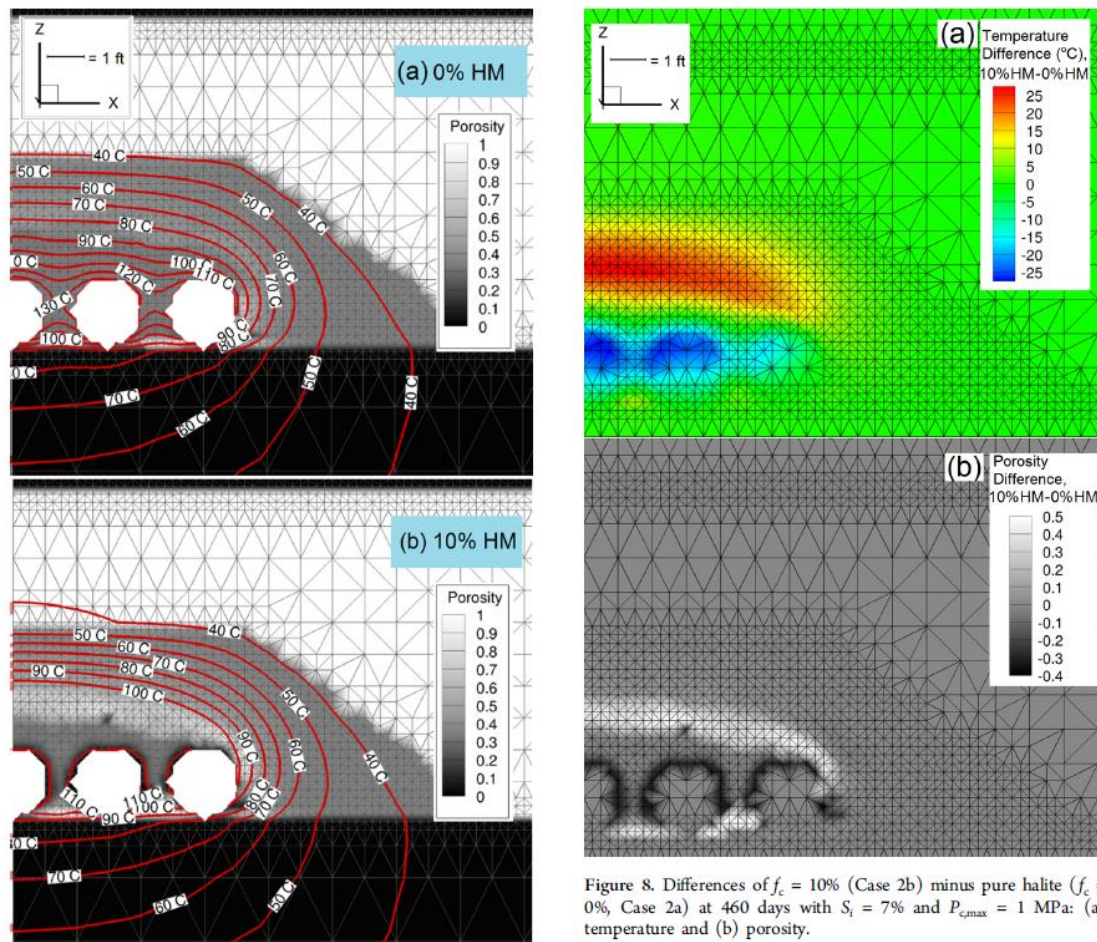


Figure 7. Porosity and temperature around the heaters at 460 days for (a) Case 2a,  $f_c = 0\%$  and (b) Case 2b,  $f_c = 10\%$ . RoM  $\phi_i = 0.35$ ,  $S_i = 7\%$ , and  $P_{c,max} = 1$  MPa.

Figure 8. Differences of  $f_c = 10\%$  (Case 2b) minus pure halite ( $f_c = 0\%$ , Case 2a) at 460 days with  $S_i = 7\%$  and  $P_{c,max} = 1$  MPa: (a) temperature and (b) porosity.

away from the waste,<sup>17</sup> leading to cooler maximum temperatures and less dry-out around the canisters. Beyond the condensation front, the higher saturations of the case with the

hydrous mineral dehydration model leads to lower thermal diffusivity and thus hotter temperatures.

The choice of  $P_{c,max}$  at zero saturation has an effect on the moisture distribution as well (case 3), as discussed in the SI (Figures S2 and S3).

**Implications for Disposal of Heat-Generating Nuclear Waste.** Depending on uncertain factors such as initial moisture content and retention properties of the RoM salt, the addition

of water from hydrous mineral dehydration may make a significant difference in final temperature, moisture, and porosity redistribution. The redistribution of mass, moisture, and temperature at early times may impact the time evolution of salt plasticity and mechanical deformation at longer time scales. Additionally, other strongly coupled thermal, hydrological, and chemical processes around heat-generating nuclear waste in bedded salt formations are modified by water released from minerals. Ongoing model development research and experimental work will improve the ability to make longer-term predictions, such as by including mechanical effects related to viscoplastic creep in the host rock and reconsolidation of the RoM salt.

■ ASSOCIATED CONTENT

📄 Supporting Information

Additional TGA analyses and simulation results. The Supporting Information is available free of charge on the ACS Publications website at DOI: 10.1021/acs.est.5b01002.

■ AUTHOR INFORMATION

Corresponding Author

\*Phone: 505-667-1049; fax: 505-665-3285; e-mail: ajordan@lanl.gov.

Notes

The authors declare no competing financial interest.

■ ACKNOWLEDGMENTS

This work was funded by the DOE Office of Nuclear Energy and Office of Environmental Management. We are grateful for reviews of drafts of this article by Mark Person, Prasad Nair, Roger Nelson, and others. Computational mesh support was provided by Carl Gable, Terry Miller, and Dylan Harp. Thanks are also due to Brian Dozier and Doug Weaver for assistance collecting samples. Finally, we thank the reviewers from this journal, whose comments led to revisions which greatly improved this paper.

■ REFERENCES

(1) Hansen, F. D.; Leigh, C. D. *Salt Disposal of Heat-Generating Nuclear Waste*; Sandia National Laboratories Report, SAND2011-0161; 2011; <http://prod.sandia.gov/techlib/access-control.cgi/2011/110161.pdf>.

(2) Bodvarsson, G. S.; Boyle, W.; Patterson, R.; Williams, D. Overview of scientific investigations at Yucca Mountain—the potential repository for high-level nuclear waste. *J. Contam. Hydrol.* 1999, 38 (1), 3–24 DOI: 10.1016/S0169-7722(99)00009-1.

(3) Neuzil, C. E. Can Shale Safely Host US Nuclear Waste? *Trans. Am. Geophys. Union* 2013, 94 (30), 261–262.

(4) Beauheim, R. L.; Roberts, R. M. Hydrology and hydraulic properties of a bedded evaporite formation. *J. Hydrol.* 2002, 259 (1), 66–88 DOI: 10.1016/S0022-1694(01)00586-8.

(5) Hansen, F. D.; Popp, T.; Wiczorek, K.; Stuhrenberg, D. *Granular Salt Summary: Reconsolidation Principles and Applications*; Prepared for U.S. Department of Energy Used Fuel Disposition, Report FCRD-UFD-2014-000590; 2014.

(6) *The Waste Isolation Pilot Plant: A Potential Solution for the Disposal of Transuranic Waste*; National Research Council: Washington, DC, 1996; <http://www.nap.edu/openbook.php?isbn=0309054915>.

(7) Kuhlman, K. L.; Malama, B. *Brine Flow in Heated Geologic Salt*; Sandia National Laboratories Report, SAND2013-1944; 2013; <http://prod.sandia.gov/techlib/access-control.cgi/2013/131944.pdf>.

(8) Mönig, J.; Beuth, T.; Wolf, J.; Lommerzheim, A.; Mrugalla, S. Development Based on a Site-Specific Features, Events and Processes

(FEP) Database-13304. In *Proceedings WM2013 Conference*, Phoenix, AZ, 2013.

(9) Istvan, J. A.; Evans, L. J.; Weber, J. H.; Devine, C. Rock mechanics for gas storage in bedded salt caverns. *Int. J. Rock Mech. Min. Sci.* 1997, 34 (3), 142.e1–142.e12 DOI: 10.1016/S1365-1609(97)00108-1.

(10) Carter, J. T.; Rodwell, P. O.; Robinson, B. A.; Kehrman, B. *Defense Waste Salt Repository Study: Fuel Cycle Research & Development*; Prepared for U.S. Department of Energy Used Fuel Disposition, Report FCRD-UFD-2012-000113; 2012.

(11) Carter, N. L.; Hansen, F. D.; Senseny, P. E. Stress magnitudes in natural rock salt. *J. Geophys. Res.: Solid Earth* 1982, 87 (B11), 9289–9300 DOI: 10.1029/JB087iB11p09289.

(12) Stein, C. L. *Mineralogy in the Waste Isolation Pilot Plant (WIPP) Facility Stratigraphic Horizon*; Sandia National Laboratories Report, SAND-85-0321; 1985; [http://www.wipp.energy.gov/library/cra/2009\\_cra/references/Others/Stein\\_1985\\_Mineralogy\\_in\\_the\\_WIPP\\_SAND85\\_0321.pdf](http://www.wipp.energy.gov/library/cra/2009_cra/references/Others/Stein_1985_Mineralogy_in_the_WIPP_SAND85_0321.pdf).

(13) Freyer, D.; Voight, W. Crystallization and phase stability of CaSO<sub>4</sub> and CaSO<sub>4</sub>-based salts. *Monatsh. Chem.* 2003, 134 (5), 693–719 DOI: 10.1007/s00706-003-0590-3.

(14) Roedder, E.; Bassett, R. L. Problems in determination of the water content of rock-salt samples and its significance in nuclear-waste storage siting. *Geology* 1981, 9 (11), 525–530 DOI: 10.1130/0091-7613(1981)9.

(15) Caporuscio, F. A.; Boukhalfa, H.; Cheshire, M. C.; Jordan, A. B.; Ding, M. *Brine Migration Experimental Studies for Salt Repositories*; Los Alamos National Laboratory Document, LA-UR-13-27240; 2013; <http://energy.gov/sites/prod/files/2013/12/fs/BrineMigrationinExpermntsSaltR1.pdf>.

(16) Shcherban, J. P.; Shirokikh, I. N. Thermodynamic and experimental data on stability of gypsum, hennihydrate, and anhydrite under hydrothermal conditions. *Int. Geol. Rev.* 1971, 13 (11), 1671–1673 DOI: 10.1080/00206817109475625.

(17) Udell, K. S. Heat transfer in porous media considering phase change and capillarity—the heat pipe effect. *Int. J. Heat Mass Transfer* 1985, 28 (2), 485–495.

(18) Doughty, C.; Pruess, K. A similarity solution for two-phase fluid and heat flow near high-level nuclear waste packages emplaced in porous media. *Int. J. Heat Mass Transfer* 1990, 33 (6), 1205–1222.

(19) Olivella, S.; Castagna, S.; Alonso, E. E.; Lloret, A. Porosity variations in saline media induced by temperature gradients: experimental evidences and modelling. *Transp. Porous Media* 2011, 90 (3), 763–777 DOI: 10.1007/s11242-011-9814-x.

(20) Krumhansl, J. L.; Stein, C. L.; Jarrell, G. D.; Kimball, K. M. *Summary of WIPP Room B Heater Test Brine and Backfill Material Data*; Sandia National Laboratories Report, SAND-90-0626; 1991.

(21) Stauffer, P. H.; Harp, D. R.; Jordan, A. B.; Lu, Z.; Kelkar, S.; Kang, Q.; Ten Cate, J.; Boukhalfa, H.; Labayed, Y.; Reimus, P. W.; Caporuscio, F. A.; Miller, T. A.; Robinson, B. A. *Coupled Model for Heat and Water Transport in a High Level Waste Repository in Salt*; Los Alamos National Laboratory Document, LA-UR-13-27584; 2013; [http://www.energy.gov/sites/prod/files/2013/12/fs/CouplModelHeatWaterTransprtGenericHLWRRepSalt\\_1.pdf](http://www.energy.gov/sites/prod/files/2013/12/fs/CouplModelHeatWaterTransprtGenericHLWRRepSalt_1.pdf).

(22) Bérest, P.; Ghoreychi, M.; Hadj-Hassen, F.; Tijani, M., Eds. *Mechanical Behaviour of Salt VII*; CRC Press: London, 2012.

(23) Olivella, S.; Gens, A. A Constitutive Model for Crushed Salt. *Int. J. Numer. Anal. Meth. Geomech.* 2002, 26, 719–746.

(24) Blanco Martín, L.; Wolters, R.; Rutqvist, J.; Lux, K.-H.; Birkholzer, J. T. Comparison of two simulators to investigate thermal–hydraulic–mechanical processes related to nuclear waste isolation in saliferous formations. *Comput. Geotechnics* 2015, 66, 219–229 DOI: 10.1016/j.compgeo.2015.01.021.

(25) Clayton, D. J.; Gable, C. W. *3-D Thermal Analyses of High Level Waste Emplaced in a Generic Salt Repository*; Sandia National Laboratories Report, SAND2009-0633P; 2009.

(26) Stone, C. M.; Holland, J. F.; Bean, J. E.; Arguello, J. G. Coupled thermal-mechanical analyses of a generic salt repository for high level

## 6. Future Work

Simulations tied to experiments have provided pathways forward to reduce uncertainty in our understanding of multiphase flow and transport in granular salt. Continued iteration between data collection and simulation will help us refine our conceptual and numerical models in anticipation of a coming field scale test of heat generating nuclear waste in geological salt deposits.

The work performed in 2014-2015 highlighted a few differences between data and simulations that are slated to be further explored in 2016. Confirming the nature of the discrepancies between the experiments and both conceptual and numerical models is a substantial effort that will reduce uncertainty during design and implementation of an in-drift disposal test.

Numerical models of the experiments show generally hotter temperatures than observed. This could be caused by several factors. One possibility is that thermal conductivity functions for the experimental material (uniform grain size pure sodium chloride) do not match the numerical parameters. Another model/data difference that is under investigation concerns advective heat transfer with the complex boiling and condensing of water and the changes in porosity and permeability structure caused by the salt dissolution. Additional research is necessary with run-of-mine salt to confirm the thermal properties of this material. Moderately heated runs, < 80 C, offer the possibility of assessing the accuracy of the thermal conductivity without the complication of large porosity changes or complex boiling and condensing fronts.

## REFERENCES

- Bechthold, W., E. Smailos, S. Heusermann, W. Bollingerfehr, B. Sabet, T. Rothfuchs, P. Kamlot, J. Grupa, S. Olivella, and F.D. Hansen. 2004. Backfilling and sealing of underground repositories for radioactive waste in salt (Bambus II project). Final Report for European Atomic Energy Community EUR 20621, Office for Official Publications of the European Communities, Luxembourg.
- Birkholzer, J.T. 2004. Estimating liquid fluxes in thermally perturbed fractured rock using measured temperature profiles. *J. Hydrol.* 327 (3-4): 496-515, doi 10.1016/j.jhydrol.2005.11.049.
- Birkholzer, J.T. and Y.W. Tsang. 2000. Modeling the thermal-hydrologic processes in a large-scale underground heater test in partially saturated fractured tuff. *Water Resour. Res.* 36(6): 1431-1447.
- Bodvarsson, G.S., W. Boyle, R. Patterson, and D. Williams. 1999. Overview of scientific investigations at Yucca Mountain—the potential repository for high-level nuclear waste. *J. Contam. Hydrol.* 38 (1): 3–24, doi 10.1016/S0169-7722(99)00009-1.
- Brady R., C. Herrick, K. Kuhlman, B. Malama, M. Schuhen, and B. Stenson. 2013. Sandia Experimental Programs Background and Targeted Activities for Forensic Investigation of Rooms B and A1. NE Milestone M4FT-13SN0818036.
- Bruckler, L., B.C. Ball, and P. Renault. 1989. Laboratory estimation of gas diffusion coefficient and effective porosity in soils. *Soil Science*, 147(1): 1-10.
- Caporuscio, F.A., H. Boukhalfa, M.C. Cheshire, A.B. Jordan, and M. Ding. 2013. Brine Migration Experimental Studies for Salt Repositories, FCRD Used Fuel Disposition Campaign Milestone FCRD-UFD-2013-000204, September 25, 2013.
- Cinar, Y., G. Pusch, and V. Reitenbach. 2006. Petrophysical and capillary properties of compacted salt. *Transp. Porous Media* 64 (2): 199-228.
- Clayton, D.J., and C.W. Gable. 2009. 3-D Thermal Analyses of High Level Waste Emplaced in a Generic Salt Repository. Sandia National Laboratories Report SAND2009-0633P. Albuquerque, NM.
- Domalski, E.S., and E.D. Hearing. Condensed Phase Heat Capacity Data. In: P.J. Linstrom and W.G. Mallard, editors, **NIST Chemistry WebBook, NIST Standard Reference Database Number 69**. National Institute of Standards and Technology, Gaithersburg, MD. <http://webbook.nist.gov> (accessed 13 July 2015).
- Doughty, C., and K. Pruess. 1990. A similarity solution for two-phase fluid and heat flow near high-level nuclear waste packages emplaced in porous media. *Int. J. Heat Mass Transfer* 33(6): 1205–1222.
- Eppelbaum, L. V., I. Kutasov, and A. Pilchin. 2014. Applied Geothermics. Springer Science + Business Media LLC, New York, NY.
- Freeze, R.A., and J.A. Cherry. 1979. Groundwater. Prentice Hall, Englewood Cliffs, NJ.
- Hansen, F.D., and C.D. Leigh. 2012. Salt disposal of heat-generating nuclear waste. Sandia National Laboratories Report SAND2011-0161. Albuquerque, NM.

- Hansen, F.D., C.D. Leigh, W. Steininger, W. Bollingerfehr, and T. Von Berlepsche. 2015. Proceedings of the 5th US/German Workshop on Salt Repository Research Design and Operation. Sandia National Laboratories Report SAND2015-0500R. Albuquerque, NM.
- Hemond, H.F., and E.J. Fechner. 1999. Chemical Fate and Transport in the Environment. Elsevier Science, Atlanta, GA.
- Ho, C.K., and S.W. Webb (Eds.). 2006. Gas transport in porous media (Vol. 20). Springer, Dordrecht, The Netherlands.
- Horita, J. 1989. Analytical aspects of stable isotopes in brines. *Chemical Geology: Isotope Geoscience section*, 79(2): 107-112.
- Jin, Y., and J.A. Jury. 1996. Characterizing the dependence of gas diffusion coefficient on soil properties. *Soil Science Society of America Journal*, 60(1): 66-71.
- Jordan, A.B., P.H. Stauffer, D.T. Reed, H. Boukhalfa, F.A. Caporuscio, and B.A. Robinson. 2014. Draft Test Plan for Brine Migration Experimental Studies in Run-of-Mine Salt Backfill. Los Alamos National Laboratory Report LA-UR-14-27338. Los Alamos, NM.
- Jordan, A.B., H. Boukhalfa, F.A. Caporuscio, and P.H. Stauffer. 2015. Brine Transport Experiments in Run-of-Mine Salt. Los Alamos National Laboratory Report LA-UR-15-26804. Los Alamos, NM.
- Jury, W.A., and R. Horton. 2004. Soil Physics, 6th ed. John Wiley & Sons, Hoboken, NJ.
- Kelly, W.R. 1985. Brine migration in salt: Topical report.  
<http://pbadupws.nrc.gov/docs/ML0404/ML040410467.pdf> (accessed 10 July 2013).
- Kelkar, S., G. WoldeGabriel, and K. Rehfeltdt. 2011. Hot Dry Rock Geothermal Energy Development at Los Alamos National Laboratory: 1970-1995, Final Report. Los Alamos National Laboratory Report LA-14433-HDR.
- Krumhansl, J.L., C.L. Stein, G.D. Jarrell, and K.M. Kimball. 1991. Summary of WIPP Room B heater test brine and backfill material data. Sandia National Laboratories Report, SAND-90-0626.
- Kuhlman, K.L., and B. Malama. 2013. Brine Flow in Heated Geologic Salt. Sandia National Laboratories Report SAND2013-1944. Albuquerque, NM.
- Lappin, A.R. 1988. Summary of site-characterization studies conducted from 1983 through 1987 at the Waste Isolation Pilot Plant (WIPP) site, southeastern New Mexico. In: Post, R.G.; High-level waste and general interest: Volume II, p. 371-376. Waste Management: Symposium on Radioactive Waste Management, Tucson, AZ, 28 Feb – 3 Mar 1988.
- Marrero, T.R., and E.A. Mason. 1972. Gaseous diffusion coefficients. *Journal of Physical and Chemical Reference Data*, 1(1): 3-118.
- Millington, R.J., and J.P. Quirk. 1961. Permeability of porous solids. *Trans. Faraday Soc.* 57: 1200–1207.
- Neuzil, C.E. 2013. Can Shale Safely Host US Nuclear Waste? *Trans., Am. Geophys. Union* 94(30): 261–262.
- Olivella, S., S. Castagna, E.E. Alonso, and A. Lloret. 2011. Porosity variations in saline media

- induced by temperature gradients: experimental evidences and modeling. *Transport in porous media*, 90(3): 763-777.
- Pollock, D.W. 1986. Simulation of Fluid Flow and Energy Transport Processes Associated With High-Level Radioactive Waste Disposal in Unsaturated Alluvium. *Water Resources Research*, 22(5): 765-775.
- Reimus, P., G. Pohll, T. Mihevc, J. Chapman, M. Haga, B. Lyles, S. Kosinski, R. Niswonger, and P. Sanders. 2003. Testing and parameterizing a conceptual model for solute transport in a fractured granite using multiple tracers in a forced-gradient test. *Water Resour. Res.*, 39(12).
- Robinson, B.A., N.Z. Elkins, and J.T. Carter. 2012. Development of a US Nuclear Waste Repository Research Program in Salt. *Nuclear Technology*, 180(1): 122-138.
- Rutqvist, J., D. Barr, R. Datta, A. Gens, A. Millard, S. Olivella, C.-F. Tsang, and Y. Tsang. 2005. Coupled thermal–hydrological–mechanical analyses of the Yucca Mountain Drift Scale Test—Comparison of field measurements to predictions of four different numerical models. *International Journal of Rock Mechanics and Mining Sciences*, 42(5): 680-697.
- Sander, R. 2015. Henry’s law constants. In: P.J. Linstrom and W.G. Mallard, editors, NIST Chemistry WebBook, NIST Standard Reference Database Number 69. National Institute of Standards and Technology, Gaithersburg, MD. <http://webbook.nist.gov> (accessed 22 April 2015).
- Silverman, T.S. 1999. A pore-scale experiment to evaluate enhanced vapor diffusion in porous media. Doctoral dissertation, New Mexico Institute of Mining and Technology.
- Stauffer, P.H., D.R. Harp, A.B. Jordan, Z. Lu, S. Kelkar, Q. Kang, J. Ten Cate, H. Boukhalfa, Y. Labayed, P.W. Reimus, F.A. Caporuscio, T.A. Miller, and B.A. Robinson. 2013. Coupled model for heat and water transport in a high level waste repository in salt; Los Alamos National Laboratory Document, LA-UR-13-27584. [http://www.energy.gov/sites/prod/files/2013/12/f5/CouplModelHeatWaterTransprtGenericHLWRepSalt\\_1.pdf](http://www.energy.gov/sites/prod/files/2013/12/f5/CouplModelHeatWaterTransprtGenericHLWRepSalt_1.pdf).
- Stauffer, P.H., A.B. Jordan, D.J. Weaver, F.A. Caporuscio, J.A. Ten Cate, H. Boukhalfa, B.A. Robinson, D.C. Sassani, K.L. Kuhlman, E.L. Hardin, S.D. Sevougian, R.J. MacKinnon, Y. Wu, T.A. Daley, B.M. Freifeld, P.J. Cook, J. Rutqvist, and J.T. Birkholzer. 2015. Test proposal document for phased field thermal testing in salt; FCRD Used Fuel Disposition Campaign Milestone FCRD-UFD-2015-000077, April 30, 2015.
- Stoller, 2014. Independent Design Analysis and Verification of Heater Canister, Final Report to Los Alamos National Security, LCC, Subcontract 253219.
- Watts, H. 1971. Temperature dependence of the diffusion of carbon tetrachloride, chloroform, and methylene chloride vapors in air by a rate of evaporation method. *Canadian Journal of Chemistry*, 49(1): 67-73.
- Zyvoloski, G.A. 2007. FEHM: A control volume finite element code for simulating subsurface multi-phase multi-fluid heat and mass transfer. Los Alamos National Laboratory Report LA-UR-07-3359. Los Alamos, NM.
- Zyvoloski, G.A., B.A. Robinson, Z.V. Dash, and L.L. Trease. 1997. Summary of the models and methods for the FEHM application—A finite element mass-and heat-transfer code. Los



Alamos National Laboratory Report LA-13307-MS, modified 1999. Los Alamos, NM.

## APPENDIX A: NGAS AND BOUN USAGE

The new usage of the *ngas* macro is given in Table 7. Annotated examples of its usage are given in Table 8. A comprehensive list of changes made to FEHM source code files is provided in **Error! Reference source not found.**

Group 1 - ICO2D			
Group 2- JA, JB, JC, PCO2			
Group 3 - JA, JB, JC, HUM_SAT, PFLOWA			
Group 4- JA, JB, JC, QCD, AIPED			
Input Variable	Format	Default	Description
ICO2D	Integer	3	Solution descriptor for <i>ngas</i>
PCO2	Real	0.	Initial partial pressure of noncondensable gas
HUM_SAT	Real	0.	Specified humidity (if > 0), specified saturation (if < 0; absolute value used for specified saturation).  If HUM_SAT = -888, then the water source/sink associated with humidity is disabled.
PFLOWA	Real	0.1	Specified total pressure. Even if HUM_SAT is disabled (-888), if PFLOWA > 0, it is enabled.
QCD	Real	0.	Specified noncondensable gas flowrate (kg/s) when AIPED = 0; noncondensable gas mass fraction when AIPED ≠ 0.
AIPED	Real	1.	Impedance factor.

Table 7. New usage of the FEHM *ngas* macro.

Example 1. Changes in <i>ngas</i> input showing new noncondensable gas mass fraction input. <i>Flow</i> macro shown for completeness.
<pre> flow 1 1 1 0.105 -30. 1.e0 6 6 1 0.10 -30. 1.e0  ngas 3 1 6 1 1.e-8 &lt;initial ngas partial pressure                  &lt; no humidity or specified saturation 1 1 1 0.99 1. &lt; if inflow, 0.99 ngas mass fraction applied, aiped = 1. 6 6 1 0.99 1. &lt; node 6, if outflow, will ignore these values and use in place values (if inflow)                     </pre>

Table 8. Annotated examples of the updated *ngas* and *boun* macros.

Example 2. Boundary conditions for ngas showing new options. Flow macro was not needed.	
ngas	
3	
1 6 1 -80	< "-80" means the initial ngas partial pressure = $P_{tot} - P_v(80)$ where $P_{tot}$ is the total pressure and $P_v(80)$ is the water vapor pressure at 80°C.
1 1 1 -0.05 0.1	< target saturation value of 0.05 , air pressure condition of 0.1
2 2 1 -888 0.1	< target saturation disabled , air pressure condition of 0.1
	< no ngas mass fraction or ngas flow rate
Example 3. Boundary conditions for ngas inputted in the boun macro. Flow macro was not needed.	
ngas	
3	
1 6 1 -80	< "-80" means the initial ngas partial pressure = $P_{tot} - P_v(80)$ where $P_{tot}$ is the total pressure and $P_v(80)$ is the water vapor pressure at 80 C.
	< no humidity input
	< no ngas mass fraction or ngas flow rate
boun	
model 1	
ti	
2 0. 5.	
pw	
0.105 0.10	< note specified pressure changed at 5 days
ft	
30. 30.	
if	
1.e0 1.e0	
fxa	
0.99 0.99	< flowing mass fraction (fxa) of ngas denoted by 'xa' , only for inflow
ts	
0.0001 0.0001	
model 2	
ti	
2 0. 5.	
pw	
0.10 0.105	< note specified pressure changed at 5 days, produces a flow reversal
ft	
30. 30.	
if	
1.e0 1.e0	
fxa	
0.001 0.001	
1 1 1 1	
6 6 1 2	

Table 8, continued.

File	Description of changes
saltctr.f	Created a general module to manage the coupled flow and chemical reactions. Described in this report. Also works with the chemistry turned off.
input.f	Added a call to SALT module saltctr.f for reading input.
allocmem.f	Added memory allocation for variable associated with new BC in ngas module.
releasemem.f	Released memory for new variables as appropriate.
co2ctr.f	Modified input to allow humidity or saturation to be fixed. Added input for flowing noncondensable gas mass fraction. Added additional conditional blocks to separate functionality.
data.f	Initialized additional arrays for the salt module and to allow for noncondensable gas mass fraction specification for inflow from pressure source.
dvacalc.f	Modified code to change the noncondensable gas diffusion coefficient from a fully implicit formulation to an explicit formulation
comdi.f	Added arrays for additional <i>ngas</i> boundary conditions and new keywords in <i>boun</i> macro. Added another permeability array for last tracer timestep for permeability averaging.
comai.f	Added more global variables required for the salt controller. Added integer variable associated with counting restarted time steps.
comfi.f	Added real the allocatable variable <i>qng</i> to store the gas flowrate.
nr_stop_ctr.f	Made corrections that allow the Newton Raphson relaxation factor to be modified when using the <i>ngas</i> keyword.
scanin.f	Added search for variables associated with new <i>boun</i> macro keyword 'fxa.' Needed for proper memory allocation.
wrtout.f	Added output to report repeated time steps, number of gridblock in each phase state, and residual for noncondensable gas mass balance. wrtout.f Added call to saltctr.f for salt output.
thrmwc.f	Added coding for new outflow BCs and added coding for additional noncondensable gas mass fraction flow conditions. See description in the report. Removed the section with the Sparrow vapor pressure model. See <i>psatl.f</i>
psatl.f	Added call to <i>vaporl_salt</i> (in <i>vaporl.f</i> ) for the fitted vapor pressure lowering function that is equivalent to the Sparrow function. See <i>vaporl.f</i> .
vaporl.f	Appended subroutine <i>vaporl_salt.f</i> which replaces the Sparrow salt related vapor pressure fit.
varchk.f	Made modification to phase change criteria for <i>ngas</i> module and added coding to restrict the maximum partial pressure of the noncondensable gas to the total pressure.
model_setup.f	Added code for reading flowing <i>ngas</i> mass fraction.
startup.f	Added additional call <i>co2ctr.f</i> to support new boundary condition setup. See <i>co2ctr.f</i> description.
fehmn_pcx.f	Removed call to <i>porosi.f</i> for salt controlled porosity update. Added calls

flow_boun.f	Added coding for specifying flowing noncondensable gas mass fraction.
flow_boundary_conditions.f	Added coding changing the flowing noncondensable gas mass fraction.
csolve.f	Added call to saltctr.f to manage porosity and permeability changes.
porosi.f	Fixed volume change calculation and moved salt-related printout to saltctr.f

Table 9. Description of changes to FEHM source code files.

## APPENDIX B: SALT CONTROLLER MODULE USAGE

Keyword *saltctr* is used to initialize the salt controller. Descriptions of the inputs that follow are provided in Table 10 to Table 15.

### KEYWORD *saltppor*

Keyword specifying type of porosity compressibility model.

Group 1 - IPOROS (only IPOROS = 6 or 7 allowed)

Group 2 - JA, JB, JC, POR1 ,POR2 ,POR3, POR4

(1 parameter entered for IPOROS = 6; 4 parameters entered for IPOROS = 7)

A warning message is written to the output file and the .err file if a salt porosity model is not entered.

NOTE: If the FEHM *trac* macro is not enabled, porosity models entered in *saltppor* will be disabled.

Table 10. Usage of keyword *saltppor*.

### KEYWORD *saltvcon*

Only one thermal conductivity model (4) is implemented for salt in the salt controller. It is based on the thermal conductivity for crushed salt (Bechthold et al, 2004).

Group 1 - IVCN(I), VC1F(I), VC2F(I) , VC3F(I), VC4F(I), VC5F(I), VC6F(I), VC7F(I), VC8F(I)

Group 2- JA, JB, JC, IVCND

A warning message is written to the output file and the .err file if a salt thermal conductivity model is not entered.

Input Variable	Format	Description
IVCN(I)	integer	model type IVCN(I) = 4 (only salt model available)
VC1F(I)	real	reference temperature (C)
VC2F(I)	real	porosity-related used in Bechthold equation
VC3F(I)	real	Coefficient of 4th order term in Bechthold equation
VC4F(I)	real	Coefficient of 3rd order term in Bechthold equation
VC5F(I)	real	Coefficient of 2nd order term in Bechthold equation
VC6F(I)	real	Coefficient of 1st order term in Bechthold equation
VC7F(I)	real	Constant term in Bechthold equation
VC8F(I)	real	Power law term in Bechthold equation
IVCND	integer	Model number to apply to nodes

Table 11. Usage of keyword *saltvcon*.

**KEYWORD *saltadif***

Group 1 - TORT

The appropriate diffusion models are TORT = 333 and TORT = 666 and are based on the Millington-Quirk model (Millington and Quirk 1961). If other models are used, a warning message is written to the output file and the .err file.

Table 12. Usage of keyword *saltadif*.

**KEYWORD *saltvapr***

Reference: Sparrow (2003). Note: The Sparrow formulation has no capillary vapor pressure lowering.

Group 1 - IVAPRSALT

Input Variable	Format	Description
IVAPRSALT	integer	IVAPRSALT = 0 - FEHM H <sub>2</sub> O vapor pressure fit with no vapor pressure lowering
IVAPRSALT	integer	IVAPRSALT = 1 - FEHM H <sub>2</sub> O vapor pressure fit with capillary vapor pressure lowering
IVAPRSALT	integer	IVAPRSALT =2 - FEHM H <sub>2</sub> O vapor pressure fit with salt-induced vapor pressure lowering
IVAPRSALT	integer	IVAPRSALT =3 - FEHM H <sub>2</sub> O vapor pressure fit with salt-induced vapor pressure lowering and capillary vapor pressure lowering

Table 13. Usage of keyword *saltvapr*.

<b>KEYWORD <i>saltnum</i></b>		
This keyword manages the updating of the nonlinear salt related variables		
Group 1 - ACTION, VALUE		
Input Variable	Format	Description
ACTION	character	Salt process to be modified ACTION = "permavg" - average permeability after every <i>tracer</i> timestep ACTION = "poravg" - average porosity after every <i>tracer</i> timestep ACTION = "pormin" - set minimum porosity
VALUE	real	parameter value related to process ACTION = "permavg", VALUE = 1-use new time step permeability VALUE = 0-use old time step permeability VALUE = 0.5-use average permeability ACTION = "poravg", VALUE = 1-use new time step porosity VALUE = 0-use old time step porosity VALUE = 0.5-use average porosity ACTION = " pormin", VALUE = minimum porosity for ppor model 7

Table 14. Usage of keyword *saltnum*.

<b>KEYWORD <i>saltend</i></b>
This keyword is used to end the salt controller.

Table 15. Usage of keyword *saltend*.